International Journal of Rock Mechanics & Mining Sciences 148 (2021) 104971

Contents lists available at ScienceDirect

International Journal of Rock Mechanics and Mining Sciences

journal homepage: www.elsevier.com/locate/ijrmms

A grain texture model to investigate effects of grain shape and orientation on macro-mechanical behavior of crystalline rock

Xianyu Zhao [a], Derek Elsworth [b], Yunlong He [a], Wanrui Hu [c], Tao Wang [a,*]

[a] State Key Laboratory of Water Resources and Hydropower Engineering Science, Wuhan University, Wuhan, 430072, Hubei, People's Republic of China
[b] Energy and Mineral Engineering & Geosciences, G3 Center and EMS Energy Institute, Penn State University, University Park, PA, 16802, USA
[c] Department of Civil Engineering, Monash University, Clayton, VIC, 3800, Australia

ARTICLE INFO

Keywords:
Grain texture model
Grain shape and orientation distribution
Lac du Bonnet granite
Particulate DEM

ABSTRACT

Grain texture characteristics play vital roles in modulating the anisotropy, strength, and ductility of crystalline rock. Grain textures (shape, size, orientation and heterogeneity) are a key parameter controlling response but are challenging to incorporate in a quantitative manner. We propose and incorporate a grain texture model (GTM) into granular mechanics modeling by the distinct element method (DEM). This model seeds then grows individual non-spherical grain clusters that honor the granular and intergranular textures of granites. The model is applied to "virtually sinter" Lac du Bonnet granite and represent the pre-through post-peak evolution of damage and deformation. The model is able to capture all significant features of this macroscopic mechanical evolution of damage through failure. With an increase in confining pressures, a transition from brittle to ductile response occurs in the post peak stage and the fitted Hoek-Brown strength envelopes for peak strength and crack-initiation stress in these numerical experiments are consistent with physical observations. An increase in aspect ratio of individual grains slightly increases the UCS/TS ratio, whereas an increase in dip angle decreases the UCS/TS ratio. Parametric studies varying the proportion of minerals and the form of contact groups with various grain shapes and orientations allow the systematic evaluation of controls of grain texture on the evolving macroscale strength and deformability. An increase in grain aspect ratio increases the proportion of inter-grain contacts. A change in dip of the grain long-axis does not change the balance of either the mineral groups or the contact groups but significantly influences the number of inter-grain tensile cracks and the resulting UCS/TS ratio.

1. Introduction

Grain texture imparted by the assemblage and interface characteristics between minerals plays a vital role in the development of microscale damage and evolution of macroscopic mechanical behavior in crystalline rocks. If such microstructure and microscopic interactions within rock can be replicated then the complex mechanical interactions contributing to macroscale behaviors may be reproduced.[1] Defining a "virtual" grain texture model (GTM) is one approach to depict the microstructure and render it amenable to numerical simulation. Three key features must be considered in the GTM: *viz.* grain geometry characteristics (size, shape and arrangement), intragrain mechanics and grain boundary interactions.

Voronoi tessellation (VT) is widely used as a tool to describe the shape of grains both for the finite element method (FEM)[2] and for discrete element method (DEM)[3–12] simulations. An advantage of DEM is that the grain boundary interactions can be readily represented with segregated contacts. There are three elements used in DEM to represent the grains present in the GTM – these are blocks, clumps, and clusters, as shown in Fig. 1. Grains represented as blocks and clumps are deformable but unbreakable. Thus, the crack modes for both blocks and clumps are limited to grain boundaries and intra-grain failure is excluded. To overcome this shortcoming, Potyondy[3] developed a grain-based model (GBM) in the two-dimensional Particle Flow Code (PFC2D) to mimic the spalling behavior of Äspö diorite by utilizing a Poisson-VT (see Fig. 1 (g)). PFC-GBM employs clusters to represent the grains, which are collections of particles, and are crushable. PFC-GBM is able to reproduce the major observations of brittle rock deformation under uniaxial compression and in Brazilian tensile tests.[13] The effects of grain size[8] and its distribution[9] is readily represented in PFC-GBM with others

; DEM, distinct element method.

* Corresponding author.
E-mail address: htwang@whu.edu.cn (T. Wang).

https://doi.org/10.1016/j.ijrmms.2021.104971
Received 10 January 2021; Received in revised form 22 April 2021; Accepted 1 November 2021

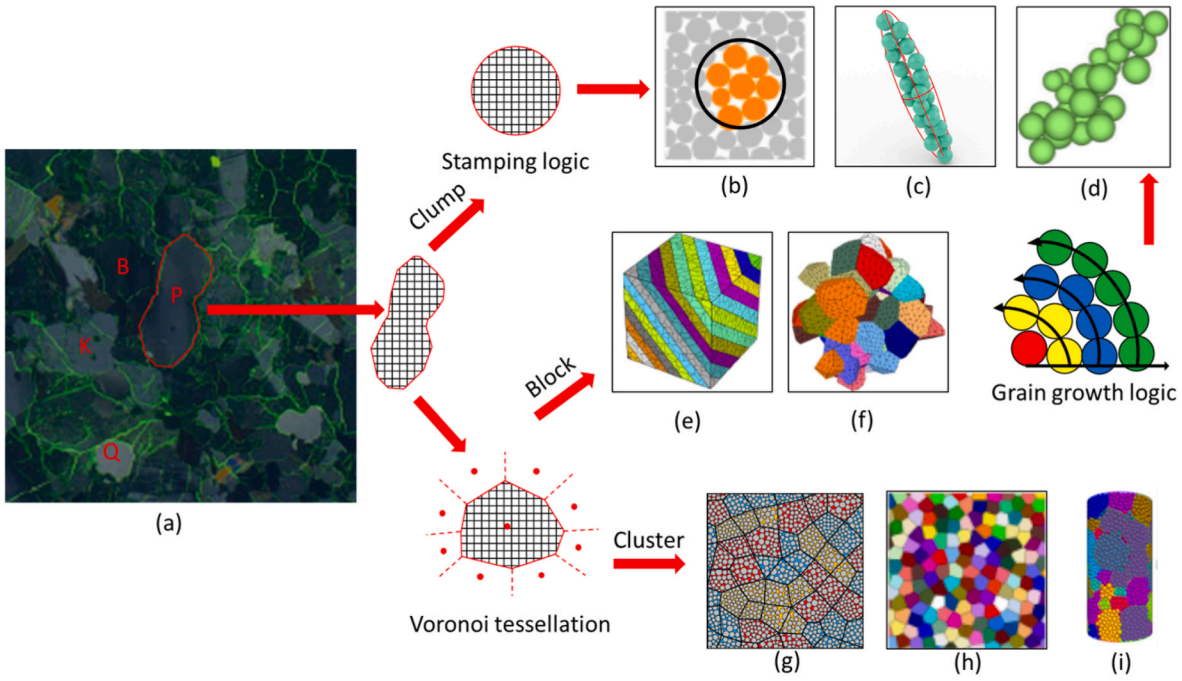

Fig. 1. Alternative methods of defining grain texture and shape in DEM: (a) Identification of grain boundary of plagioclase in Lac du Bonnet granite (white grains are quartz (Q), light grey grains are alkali feldspar (K), dark grey grains are plagioclase (P) and black grains are biotite (B), as modified from Åkesson[18]); Stamping logic for a "clump": (b) Circular stamp,[15] (c) Non-spherical stamp, modified from Zhang, et al.,[16] (d) Grain growth algorithm, modified from Ye, et al.[17] with Voronoi tessellation logic used in blocks: (e) Angular VT,[4] (f) 3D Poisson-VT,[7] and in clusters: (g) Poisson-VT,[8] (h) Imported grain geometry,[10] (i) Weight VT.[11]

improving various grain generation methods[10] (see Fig. 1(h)) and applying new contact models.[12] New VT algorithms have been proposed to control grain subdivision and grain shapes in the block based DEM[4,7] (see Fig. 1(e) and (f)) and the particulate DEM[11] (see Fig. 1(i)).

In reality, grain shapes of minerals are irregular and not always amenable to representation as standard polygons or polyhedral defined by the VT – especially where there is strong grain interlocking within the grain texture. A clump is an inseparable aggregate of particles and can be regarded as a block of any shape. A clumped particle model was proposed by Cho, et al.[14] to improve the presicion of particulate DEM models in defining macro-scale properties in both compression and tension. A stamping logic, introduced by Yoon, et al.,[15] is a typical clump generation algorithm to randomly stamp a circular contour on clumps of bonded particles (see Fig. 1(b)). However, grain shape is not always circular or spherical, and grain orientation cannot be independently considered in this case. Zhang, et al.[16] proposed a non-spherical stamping logic in 3D, which employs an ellipsoid to define the clump shape (see Fig. 1(c)). The advantage of an ellipsoidal shape is that the grain orientation can be defined by the dip angle of the long axis and a realistic value of aggregate strength may be applied. To achieve a more realistic arrangement of clumps, a 3D clump method was developed to represent the grain growth process by Ye, et al.[17] (see Fig. 1(d)). Although clumped particle models can reproduce the interaction between several minerals, there is generally no consideration of the mechanism of intra-grain breakage and interactions of multiple materials.

Intra-grain failure can be considered in bonded particle models (BPMs) where individual grains are arranged in clusters. Thus, BPMs are widely used to represent cemented materials.[19,20] As one form of BPMs, linear parallel bonded models (LPBMs) may be considered as a "cement" to collect the intragranular particles.[3,5,8–10] Conversely, the ratio of uniaxial compressive strength (UCS) to tensile strength (TS) of minerals cannot be exactly captured by LPBM. Thus, another BPM, the flat-joint model (FJM), developed by Potyondy,[21] has been used to model the contact between mineral grains.[12]

Minerals are typically more easily broken on grain boundaries than through the mineral grains. A smooth joint model (SJM) has been employed to describe the opening and sliding behavior of grain boundaries.[3,4,8,9,12,17] However, there are two reasons that the SJM is incapable of reproducing the mechanical behavior of grain boundaries. Firstly, SJM is merely fit to mimic the mechanical behavior of existing joints as it provides a sliding plane with a fixed joint angle.[22] The fixed joint plane limits the deformability of the grain shape, so it cannot provide a realistic contact for relatively large relative displacements of the grain boundaries. Secondly, due to the interlocking problem of SJM,[23] it results in an increase in shear strength and dilation angle of the joint.[10,23] Li, et al.[10] provided, instead, a strategy of using a weak LPBM to mimic the behavior of grain boundaries. A common problem existing in the current implementation of PFC-GBM is that only one kind of bond parameter is used on the grain boundaries although there are several materials present in the rock specimens.

The following develops a method of grain texture generation based on a principle of grain seeding, growth and coalescence. The novel approach considers grain shape and orientation and is executed after the grain seeding initiates and before grain clusters are developed. Multiple material interactions are considered after GTM generation. The method is then used to study the mechanical behavior of Lac du Bonnet granite under unconfined and confined compression, as measured in laboratory experiments. Once validated, parametric studies explore the effect of grain shape and orientation at microscale on macroscale deformation characteristics.

2. Grain Texture Model (GTM)

Grain texture is observed in crystalline rocks and results from the intergrowth of grains and their boundaries. A synthetic mixture of several minerals may be distinguished by its GTM. Two different contact models are selected as representations of intragrain texture and the grain boundary. A generation procedure and multiple material interactions of GTM are introduced here.

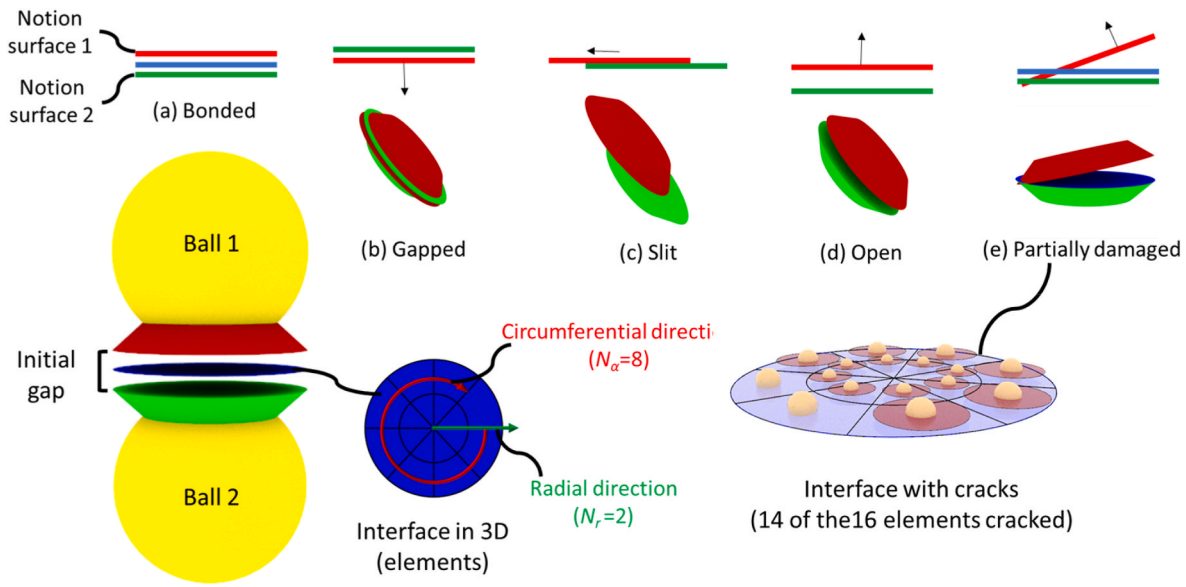

Fig. 2. Initial microstructural forms for flat joints: (a) Bonded; (b) Gapped; (c) Slit. Note that the forms of damage to a bonded flat joint: (d) Open; (e) Partially damaged with cracks colored red/blue for tensile/shear failure (modified from Potyondy[19]). (For interpretation of the references to color in this figure legend, the reader is referred to the Web version of this article.)

2.1. Intragrain texture

Deformation, dislocation, and fracture separately represent the elastic, plastic, and failure behaviors of a single grain. In PFC, BPMs are employed to mimic the aggregate of particles that constitute a single grain[24] so that they can effectively simulate intra-grain fracture by bond breaking. As one particular form of BPM, LPBMs are widely used to reproduce the mechanical behavior of brittle rock. However, due to the contribution of rotational moments, the ratio between UCS and TS is typically insufficiently large when using LBPM as a material contact model.[20] This is because, the coordination number of any particle is too small, then the solution is to increase the degree of grain interlocking by augmenting the interaction range[25] or number[3,14,26] of grains. Adoption of a flat joint model (FJM) can increase the interaction number for grains, and this may be successfully applied to represent intragranular contact for the mineral.[12]

A flat joint is a disc interface in three dimensions between two notional surfaces of grains when the FJM is installed. The interface is discretized into elements along the radial (N_r) and circumferential (N_α) directions, respectively.[27] The flat joint can be partially damaged since

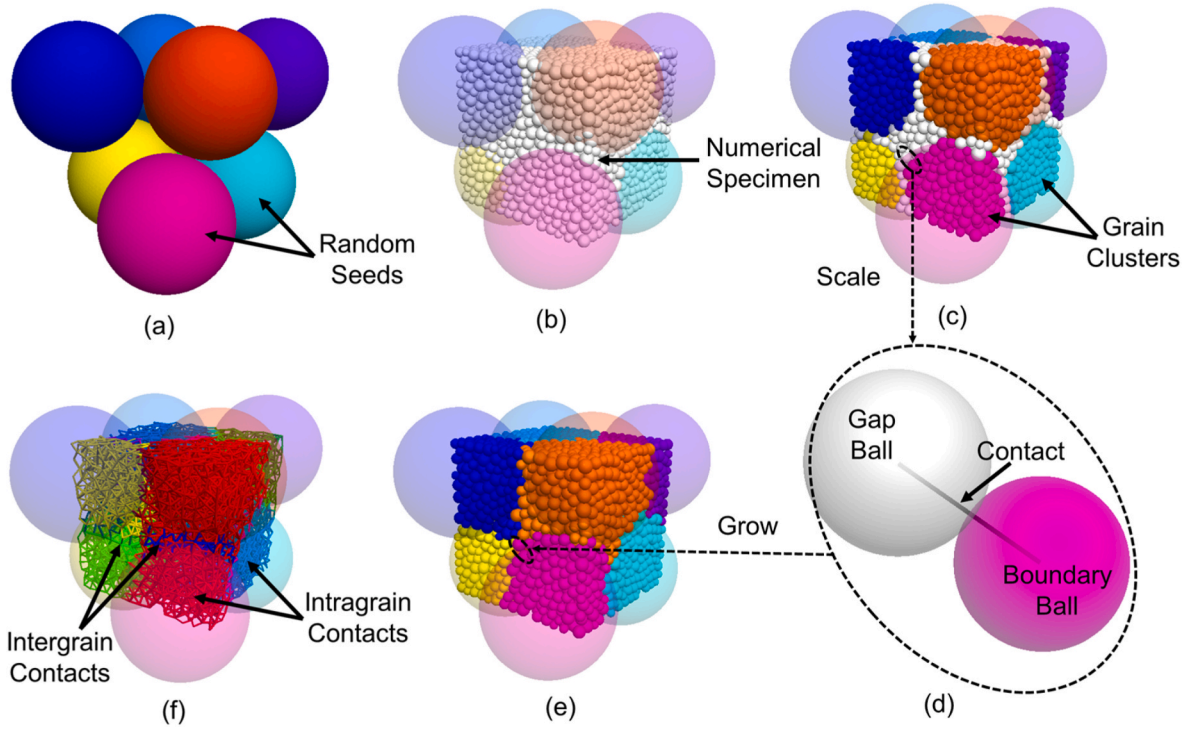

Fig. 3. Generation procedure of GTM: (a) Random grain seed distribution; (b) Numerical specimen generation; (c) Grain cluster masking; (d) Contact between gap ball and boundary ball, scaled from (c); (e) Grain cluster growth; (f) Contact grouping.

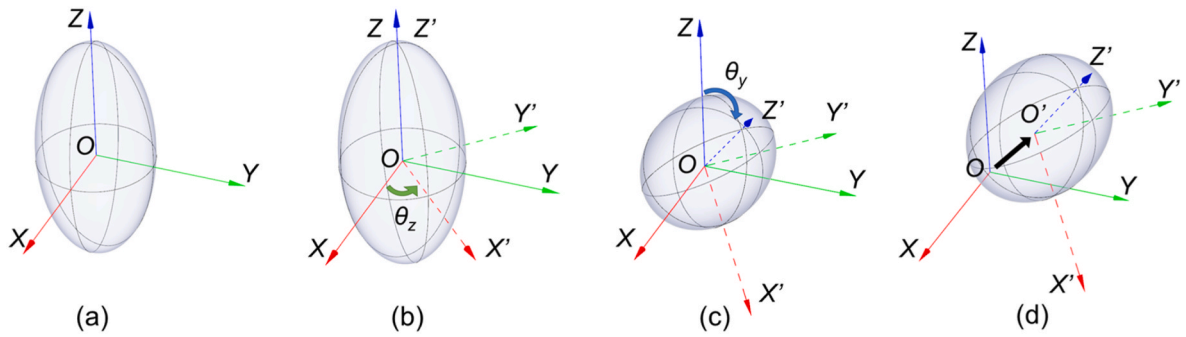

Fig. 4. Procedure of coordinate system translation: (a) Original coordinate system; (b) Rotation around the z-axis with rotational angle θ_z defining the dip direction of the ellipsoid; (c) Rotation around the y-axis, the rotational angle θ_y is also the dip angle of the ellipsoid; (d) Translation from the origin O to origin O'.

each element can be bonded or unbonded. Once the stress acting on the bonded element exceeds either the tensile or shear strength, a tensile or shear crack will occur. In its unbonded state, three initial microstructures of gapped, slit and undefined forms are defined by the nature of the initial surface gap.[21] When the initial surface gap is equal to zero, the slit contact will slide along the flat joint without rotational resistance, as shown in Fig. 2. The FJM also responds to the action of both force and moment.

2.2. Grain boundaries

Opening, sliding or rotation can occur at the grain boundaries. The grain-based model (GBM) employs a smooth joint model (SJM) to mimic the behavior of the grain boundary.[3] Because of the disadvantages of the SJM, Li, et al.[10] used a weak LPBM to mimic the behavior of grain boundaries. We follow their work and choose the LPBM as the contact model for grain boundaries.

A bond is a parallel connection with a linear component referenced as a parallel bond. Two components share the same displacement to maintain geometric compatibility in a contact and the forces on them constitute the contact force. Both components respond through the elastic micromechanical parameters of elastic modulus and stiffness ratio. Only the linear component provides the coefficient of friction to preclude the possibility of slip. The parallel bond will be broken once the normal or shear force and moment reach the maximum value of tensile or shear strength, as follows

$$\sigma_t^* = \frac{F_n}{A} + \beta\frac{M_b R}{I},\quad \tau^* = \frac{F_s}{A} + \beta\frac{M_t R}{J}(\text{For 3D})\quad \text{with } \beta \in [0,1] \tag{1}$$

where, σ_t^* and τ^* are tensile and shear strengths, F_n and F_s are normal and shear contact forces, M_b and M_t are bending and twisting moments, β is the moment contribution coefficient, and A is the contact area.

The moment contribution coefficient β can be neglected when LPBMs represent grain boundaries. The reason is that grain boundaries cannot transmit the effect of moments (the thickness of the bond is assumed to be zero), and the same pattern is set in the SJMs. The parallel bond is degraded to a cohesive interface while the moment contribution coefficient is set to be 0. Thus, the tensile or shear strength can be expressed as:

$$\sigma_t^* = \frac{F_n}{A},\quad \tau^* = \frac{F_s}{A} \tag{2}$$

2.3. Generation procedure

Contracted with VT method of the GBM and stamping logic of the clump particles method, the GTM is generated by spherical/non-spherical grain clusters and expanding the clusters to form the grain boundaries just like the grain growth process. The generation of GTMs can be divided into four steps: random grain seed distribution, numerical specimen generation, grain cluster masking and growth, and contact grouping and materials assignment, as shown in Fig. 3.

Step 1. Random Grain Seed Distribution.

Before GTM generation a mineralogical analysis defines the proportions of minerals and their size distribution. The volume fraction and grain size statistics of each mineral component is evaluated and used to distribute random grain seeds within the PFC model, as shown in Fig. 3 (a). The diameters of grain seeds are defined by the average grain sizes according to their mineral types. This standard procedure is executed by using the FISH tank package *fistpkg26* provided by Potyondy.[28] A minor modification is added before the final stage to eliminate floating particles.[29] After the distribution of grain seeds, the information including position and size of grain seeds is exported to a file.

Step 2. Numerical Specimen Generation.

A numerical specimen is generated, composed of small particles as components for the evolving clusters, as shown in Fig. 3(b). These small particles represent sub-grains within the mineral grains that will develop with their size limited by the minimum size of the mineral grains. The contact properties between small particles are initially set to one mineral material, which is the hardest mineral in the rock (as indexed by the larger effective).

Step 3. Grain Cluster Masking and Growth.

An information file containing the position and size of grain seeds is imported and grain clusters are masked in the numerical sample. The grain clusters are ellipsoidal,[16] with the direction of the long axis expressed as a dip direction θ_z and dip angle θ_y, as shown in Fig. 4. The other two short axes are considered of equivalent length with the volume equivalent to the volume of the original sphere (grain seed).

The ellipsoid is defined through a rotational coordinate system. For example, the center of an ellipsoid is located at (x_0, y_0, z_0), and the rotation angles around the x-, y- and z-axes are θ_x, θ_y and θ_z, respectively. The rotational matrixes $\mathbf{R_x}$, $\mathbf{R_y}$ and $\mathbf{R_z}$ are expressed as

$$R_x = \begin{pmatrix} 1 & 0 & 0 \\ 0 & \cos(\theta_x) & -\sin(\theta_x) \\ 0 & \sin(\theta_x) & \cos(\theta_x) \end{pmatrix},\quad R_y = \begin{pmatrix} \cos(\theta_y) & 0 & \sin(\theta_y) \\ 0 & 1 & 0 \\ -\sin(\theta_y) & 0 & \cos(\theta_y) \end{pmatrix},\quad R_z = \begin{pmatrix} \cos(\theta_z) & -\sin(\theta_z) & 0 \\ \sin(\theta_z) & \cos(\theta_z) & 0 \\ 0 & 0 & 1 \end{pmatrix} \tag{3}$$

A point (x, y, z) is defined on the ellipsoid, and the corresponding coordinates in the rotated system are (x', y', z'), thus the coordinate transformation can be expressed as

$$\begin{pmatrix} x' \\ y' \\ z' \end{pmatrix} = R_z R_y \begin{pmatrix} x - x_0 \\ y - y_0 \\ z - z_0 \end{pmatrix} \tag{4}$$

If the radii of the ellipsoid are a, b and c, the coordinates (x', y', z') must satisfy Eq. (5). The radius of the original particle is R, and the reduced radius ratio of the short axis is λ, thus

$$\left(\frac{x'}{a}\right)^2+\left(\frac{y'}{b}\right)^2+\left(\frac{z'}{c}\right)^2=1 \quad \text{with} \quad a=\lambda^2 R,\ \ b=c=\lambda^{-1}R \tag{5}$$

The aspect ratio (AR) between the long and short axes is used as an index of grain anisotropy, defined as below [30]

$$\mathrm{AR}=a/b=\lambda^2/\lambda^{-1}=\lambda^3 \quad \text{So,}\ \ \lambda=(\mathrm{AR})^{1/3} \tag{6}$$

However, gaps will exist between the grain clusters so some particles are not grouped to any grain clusters - identified as "gap balls", as shown in Fig. 3(c). A concept of "Grain Growth" is introduced.[17] The grain clusters grow along the contacts of their boundary. Once a particle belonging to a grain cluster contacts a gap ball, that automatically defines the boundary of a grain cluster, and this is then referenced as a "boundary ball", as shown in Fig. 3(d). The gap ball will be assigned the same group name as that of the boundary ball and the grain boundary will therefore extend. This growth step is executed several times until all particles belong to grain clusters, as shown in Fig. 3(e).

Step 4. Contact Grouping and Materials Assignment.

After the generation of the rock specimen containing grain clusters, contacts are grouped to assign the mechanical properties of various minerals. The rule for a contact group is based on the group names of particles at the end of a contact. According to the kinds of minerals (S), the total number of contact groups is $S(S+1)/2$.

It is determined whether the material group names of two particles at the ends of the contact are the same or not, as shown in Fig. 3(f). Once the material group names are different, the contact is in the grain boundaries of various materials. When the material group names are the same, the contact is determined whether the particle group names inherited from the IDs of grain seeds are the same (intragrain) or not (grain boundary). Material properties are assigned at the contact according to the contact group name.

As mentioned earlier, the proposed GTM is a combination of the LPBM and FJM. FJMs are directly assigned with the material properties. LPBMs are assigned with the mechanical properties according to the material group names of particles associated with them.

2.4. Multiple material interactions

The interactions of multiple materials are considered by taking the harmonic mean of the contacting materials (see Appendix). The properties on the grain boundaries are weaker than those in the grains with this achieved by multiplying by an attenuation coefficient as

$$E_c=\alpha_E\frac{2E_1E_2}{E_1+E_2},\ \ E_b=\alpha_E\frac{2E_{b,1}E_{b,2}}{E_{b,1}+E_{b,2}},$$
$$k_c=\alpha_k\frac{k_1E_2+k_2E_1}{E_1+E_2},\ \ k_b=\alpha_k\frac{k_{b,1}E_2^p+k_{b,2}E_{b,1}}{E_{b,1}+E_{b,2}}, \tag{7}$$
$$\mu_c=\min(\mu_1,\mu_2)$$

where $E_c, k_c, \mu_c, E_b, k_b$ are effective modulus, normal to shear stiffness ratio, friction coefficient, bonded modulus and bonded stiffness ratio of the contact, respectively; E_i, k_i, μ_i, $E_{b,i}$, $k_{b,i}(i=1,2)$ are effective modulus, normal to shear stiffness ratio, friction coefficient, bonded modulus and bonded stiffness ratio of ball 1 or 2 contacted in the contact, respectively; α_E and α_k are the attenuation coefficients of effective modulus and normal to shear stiffness ratio, respectively.

The strengths of bonded segments are also reduced by the mean values of the two contacting materials and multiplied by the attenuation coefficients as

Table 1
Input parameters and descriptions for the GTM.

Group classification	Microscale parameters	Symbol (units)
Random grain seed group	Number of minerals	N_m
	Proportion of minerals	C_m (%)
	Minimum particle diameter of minerals	D_{min} (mm)
	Maximum particle diameter of minerals	D_{max} (mm)
Sub-grain group	Aspect ratio	λ
	Dip direction of sub-grain	θ_z
	Dip angle of sub-grain	θ_y
	Minimum particle radius of sub-grain	R_{min} (mm)
	Ratio of particle radius of sub-grain	R_{max}/R_{min}
	Modulus of sub-grain	E* (GPa)
	Stiffness ratio of sub-grain	k^*
Material group	Effective density of material	ρ (kg/m^3)
	Effective modulus of material	E_c (GPa)
	Normal to shear stiffness ratio of material	k_c
	Friction coefficient of material	μ_c
	Bonded effective modulus of material	E_b (GPa)
	Bonded normal to shear stiffness ratio of material	k_b
	Bonded tensile strength of material	$\sigma_{t,b}$ (MPa)
	Bonded cohesion of material	C_b (MPa)
	Friction angle of material	φ_b (°)
Material-interaction group	Modulus coefficient	α_E
	Normal to shear stiffness ratio	α_k
	Friction coefficient	α_μ
	Tensile strength coefficient	α_t
	Cohesion coefficient	α_C
	Friction angle coefficient	α_φ

$$C_b=\frac{1}{2}\alpha_c(C_1+C_2),$$
$$\varphi_b=\frac{1}{2}\alpha_\varphi(\varphi_1+\varphi_2), \tag{8}$$
$$\sigma_{t,b}=\frac{1}{2}\alpha_t(\sigma_{t,1}+\sigma_{t,2})$$

where $C_b, \varphi_b, \sigma_{t,b}$ are cohesive strength, internal frictional angle and tensile strength of the contact, respectively; $C_i, \varphi_i, \sigma_{t,i}(i=1,2)$ are cohesive strength, internal frictional angle and tensile strength of ball 1 or 2 contacted in the contact, respectively; α_C, α_φ, and α_t are the attenuation coefficients of cohesive strength, internal frictional angle and tensile strength, respectively.

All the related property parameters are summarized in Table 1. Those can be classified into four groups, namely: random grain seed, sub-grain, material and material-interaction groups. Parameters in random grain seed groups are used to generate the random position and size of grain seeds. Sub-grain groups contain all parameters to generate the numerical specimen and specify the grain clusters. Material groups define the micro-mechanical properties of each mineral and material-interaction groups determine the micro-mechanical properties at grain boundaries.

3. Parameter Calibration for Lac du Bonnet granite

Lac du Bonnet (LdB) granite is a suitable material to apply the GTM since it is typically a medium to coarsely grained crystalline rock and a wealth of classical laboratory and in situ test data are available[31–33]

Table 2
Physical and macro-mechanical parameters for LdB granite.

Density ρ (kg/m^3)	Young's modulus E (GPa)	**Poisson's ratio ν**	Friction coefficient μ
2640	69–71	0.26	0.6
UCS σ_c (MPa)	TS σ_t(MPa)	Material parameter m	
200 ~ 228	9.3–13.4	28–34	

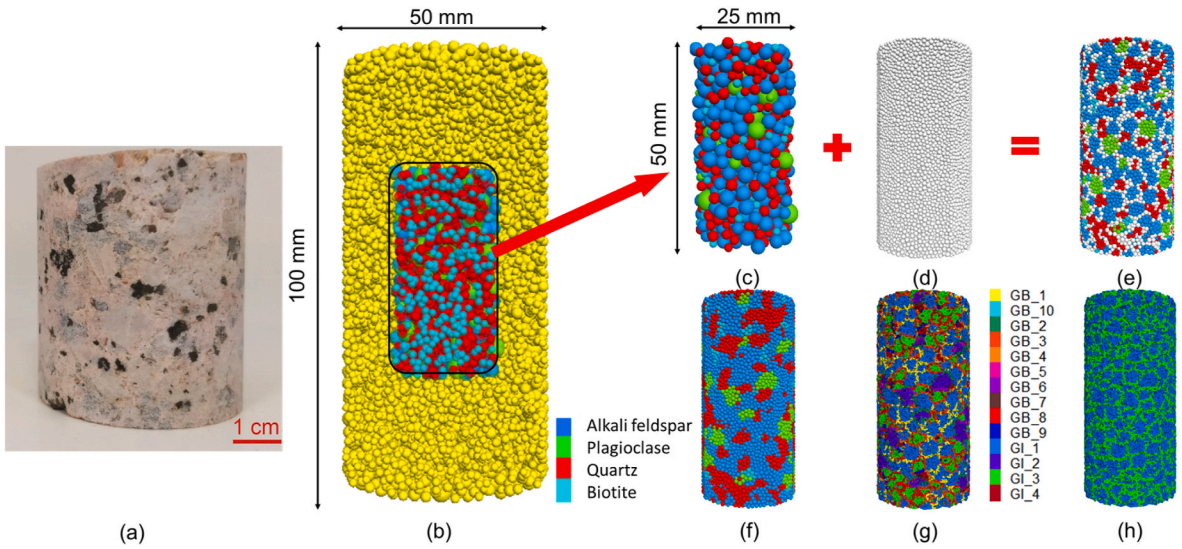

Fig. 5. Generation procedures for fabrication of LdB granite grain texture model (GTM): (a) Granite (modified from Nicco, et al.[41]); (b) Distribution of random seeds; (c) Core specimen containing random seeds; (d) Numerical Specimen; (e) Grain clusters and gap balls (white balls); (f) Grain growth and grain boundary formation; (g) Distribution of contact groups where 'GB' represents a grain boundary contact and 'GI' represents intragranular contacts; (h) Distribution of contact model, the green is the linear parallel bonded model (LPBM) and the blue is the flat joint model (FJM). (For interpretation of the references to color in this figure legend, the reader is referred to the Web version of this article.)

including that used to calibrate and validate DEM models.[3,14,17,27,34] LdB granite is a brittle rock comprising four main minerals: alkali feldspar (48%), plagioclase (17%), quartz (29%), and mica (6%, mainly biotite), with mean grain diameters of each mineral as 4, 4, 2, and 1 mm, respectively.[33] A series of laboratory and in situ experiments have been conducted by Martin,[31] with the physical and macro-mechanical parameters of the granite summarized in Table 2.

3.1. Modeling LdB granite

For computational efficiency, the GBM cannot adopt the standard experimental size of the physical rock specimens (100 mm (height) and 50 mm (width)), but instead adopts a reduced size.[8] The reduced model size does not have a significant effect on the measured strength nor the relative numbers of each crack type, effectively only changing the total number of cracks.[13] Thus, we select the size of the numerical specimen as 50 mm (height) by 25 mm (width). The diameters of the mineral grain seeds are alkali feldspar (3–4 mm), plagioclase (2–6 mm), quartz (2–3 mm), and biotite (2 mm). The minimum particle size of the numerical specimen is determined by the minimum grain diameter of the seed - a value of 0.7 mm may be appropriate with a ratio of maximum to minimum particle size of 1.66. Based on the above, the number of particles comprising the numerical specimen is 36,528. A numerical uniaxial compression test executed on a CPU i7-10700 (4.6 GHz turbo boost of all cores) lasts more than 20 h.

Aspect ratio has a significant effect on the macroscopic strength of rock,[35] as noted by He, et al.[36] Due to the various physical cleavage structures of minerals, the characteristic aspect ratios of alkali feldspar, quartz and biotite are different. Plagioclase is similar to alkali feldspar,[37] and the aspect ratios of various minerals in granites are generally of the order: plagioclase/alkali feldspar 1.4–1.9[38], biotite 1.7–2.1[38], and quartz 2–4.[39]The average aspect ratio of grains is always used to evaluate the gain shape. The average aspect ratio of granite is 1–2.5.[40] Initially, the average aspect ratio of GTM is set to be 1.0, and the gain shape is assumed to be spherical (the only condition can be considered in GBMs). The generation procedure for the LdB granite GTM is presented in Section 2 and shown schematically in Fig. 5.

3.2. Parameter calibration

Calibration procedures for the GTM are similar to the methods recommended by Zhou, et al.[12] There are two stages in the calibration procedure: (i) calibration of the FJM parameters for the material group followed by (ii) calibration of grain boundary parameters for the material-interaction group.

Stage 1: Calibration of the FJM parameters for the material group.

The calibration models for the material group are built based on the size of the numerical specimen. Three key macro-mechanical parameters are chosen to be the calibration targets - these are Young's modulus (E), uniaxial compressive strength UCS (σ_c), and tensile strength TS (σ_t).[12]

Firstly, the Young's modulus (E) and Poisson's ratio (v) are calibrated by setting large strengths.[24] Poisson's ratio is mainly determined by the selection of the normal-to-shear stiffness ratio (k_c), and here k_c of each mineral is set to be 1.6, 1.6, 1.0 and 2.0 according to the lateral deformation of alkali feldspar, plagioclase, quartz, and biotite, respectively.[5,8,10,42] Young's modulus is mainly determined by the combined action of the linear elastic modulus and the bonded elastic modulus.

Secondly, the macroscale tensile strength is calibrated by tuning the bonded tensile strength of the FJM.[27] The macroscale tensile strength is less related to either the bonded cohesive strength and bonded frictional angle, but the bonded tensile strength has a significant influence on UCS.

Finally, UCS is calibrated by adjusting bonded cohesive strength of the FJM while the bonded frictional angle is initially set to be 0°. The bonded friction angle has little effect on the UCS and is mainly related to the confined strength, hence it is calibrated by the results of the confined compression tests.

Stage 2: Calibration of grain boundary parameters for material-interaction group.

The GTM is calibrated in this stage and all parameters of the material-interaction group are initially set to be unity. The macro-mechanical parameters of the LdB granite, including E, v, σ_c, σ_t and Hoek-Brown model parameter m, are used to calibrate the attenuation coefficients of the grain boundary. Although the calibration procedure is a trial-and-error process,[8,12] several empirical relations are observed and utilized:

Table 3
Physical and calibrated macroscopic properties of four minerals in granitic rock.

Properties	Minerals			
	Plagioclase	Alkali feldspar	Quartz	Biotite
Density (kg/m^3)[12]	2600	2600	2650	2850
Young's modulus E (GPa)[13,47]	60–95	50–80	65–109	35–180
(Calibrated E)	**(78.5)**	**(71.5)**	**(96.9)**	**(50.9)**
TS σ_t (MPa)[13]	35	11–35	30–50	5–40
(Calibrated σ_t)	**(35.3)**	**(27.4)**	**(46.1)**	**(16.5)**
UCS σ_c (MPa)[10,12]	180–450	180–450	200–700	80–260
(Calibrated σ_c)	**(254.6)**	**(233.4)**	**(418)**	**(122.2)**
Calibrated m	**20**	**20**	**25**	**15**

1. Poisson's ratio (ν) of the LdB granite is mainly calibrated by the values of α_k. The normal and lateral stiffnesses at the grain boundaries are smaller than those intra-grain, thus α_E is reduced from 1 and α_k should be greater than 1.
2. Tensile strength TS (σ_t) of the LdB granite is calibrated by tuning the value of α_t to the results of the direct tension test.
3. Unconfined compressive strength UCS (σ_c) is controlled by the values of α_C and α_φ. The Hoek-Brown model parameter m is mainly related to the value of α_φ.

3.3. Calibration results

The physical and macro-mechanical properties of minerals are defined elsewhere[43–47] and are compiled by Li, et al.[10] and Zhou, et al.[12]

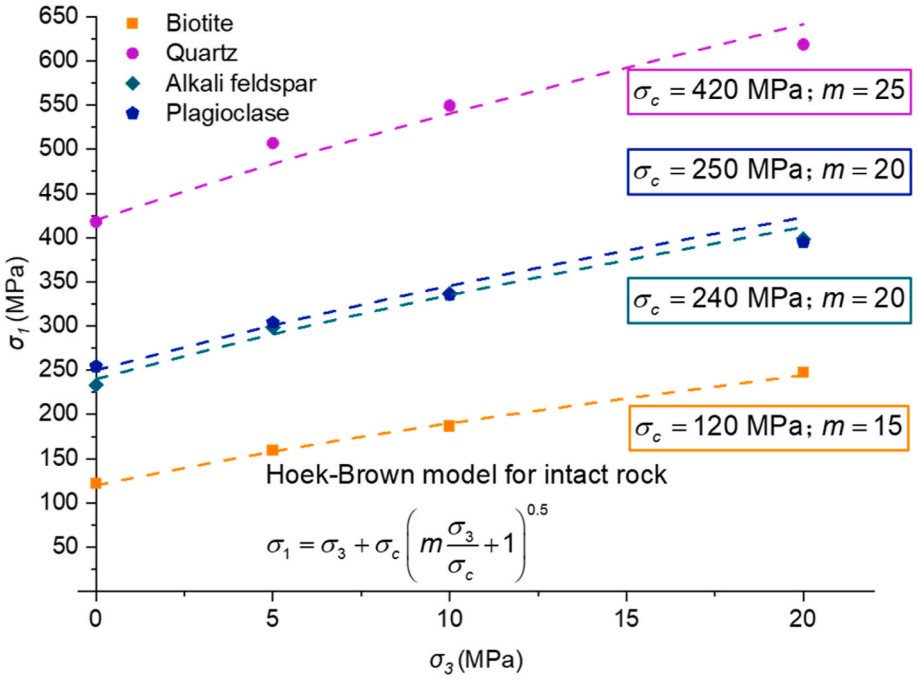

Fig. 6. Peak stresses (σ_1) in compression tests with various confining pressures (σ_3) for four major minerals (dashed lines are the fitted Hoek-Brown failure curves). (For interpretation of the references to color in this figure legend, the reader is referred to the Web version of this article.)

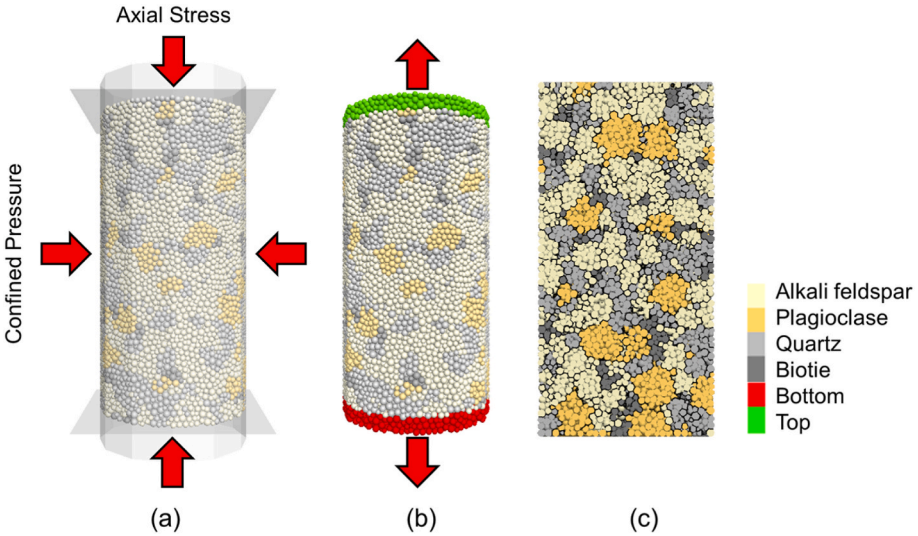

Fig. 7. Grain texture models (GTM) simulated for: (a) compression tests, and (b) direct tension tests (the thicknesseses of the top and bottom discs in the direct tension tests are 2.5 mm), and (c) axial-diametral cross section.

Table 4
Microscopic properties of four minerals and their grain boundaries.

Microscale parameters	Values			
	Plagioclase	Alkali feldspar	Quartz	Biotite
C_m (%)	17	48	29	6
D_{min} (mm)	2	3	2	2
D_{max} (mm)	6	4	3	2
ρ (kg/m^3)	2600	2600	2650	2850
E_c (GPa)	55	48	58	40
k_c	1.6	1.6	1.0	2.0
μ_c	0.6	0.6	0.6	0.6
E_b (GPa)	55	48	58	40
k_b	1.6	1.6	1.0	2.0
$\sigma_{t,b}$ (MPa)	50	40	58	26
C_b (MPa)	174	188	292	90
φ_b (°)	50	50	60	40
N_m	4			
Λ	1.0			
θ_z	0°			
θ_y	0°			
R_{min} (mm)	0.35			
R_{max}/R_{min}	1.66			
E^* (GPa)	58			
k^*	1.0			
α_E	0.9			
α_k	2.0			
α_μ	1.0			
α_t	0.25			
α_C	0.7			
α_φ	1.0			

The physical macro-mechanical properties of minerals are listed in Table 3. A small model is generated for the first calibration stage,[12] which is assembled from approximately 2000 particles with minimum radii of 0.7 mm and a particle size ratio of 1.66. The size of the small model is scaled down in the same proportion to the numerical specimen, which is 20 mm (height) by 10 mm (width). Here, the FJM is assigned in the contact model. The numbers of elements along the radial (N_r) and circumferential (N_α) directions are set to be 1 and 3, respectively. The initial surface gap is set to 0.0, denoting that a contact will be built only if two particles just touch each other. Compression and direct tension numerical tests are employed to calibrate the macro mechanical behaviors of all minerals, and the results are listed in Table 3 and Fig. 6. The calibrated results of four major minerals in the granite during the first stage are within the range mentioned in previous literature.[31–33]

After the material properties of all minerals are calibrated, a GTM is generated and used to calibrate grain boundary parameters. Models for both compression and direct tension numerical tests are shown in Fig. 7 (a) and (b), with a longitudinal cross section selected through the center of the specimen (see Fig. 7(c)). The microscale properties of the grain boundaries are listed in Table 4. The top and bottom material groups shown in Fig. 7(b) belong to a different material group from the cylindrical sample, and there are no changes of contact properties in these groups.

The stress-strain curve under uniaxial compression is shown in Fig. 8. This includes[32] four stages of the stress-strain curve pre-peak strength representing successive stages of, crack closure, an elastic region, stable crack growth, and unstable crack growth. The crack closure stage is

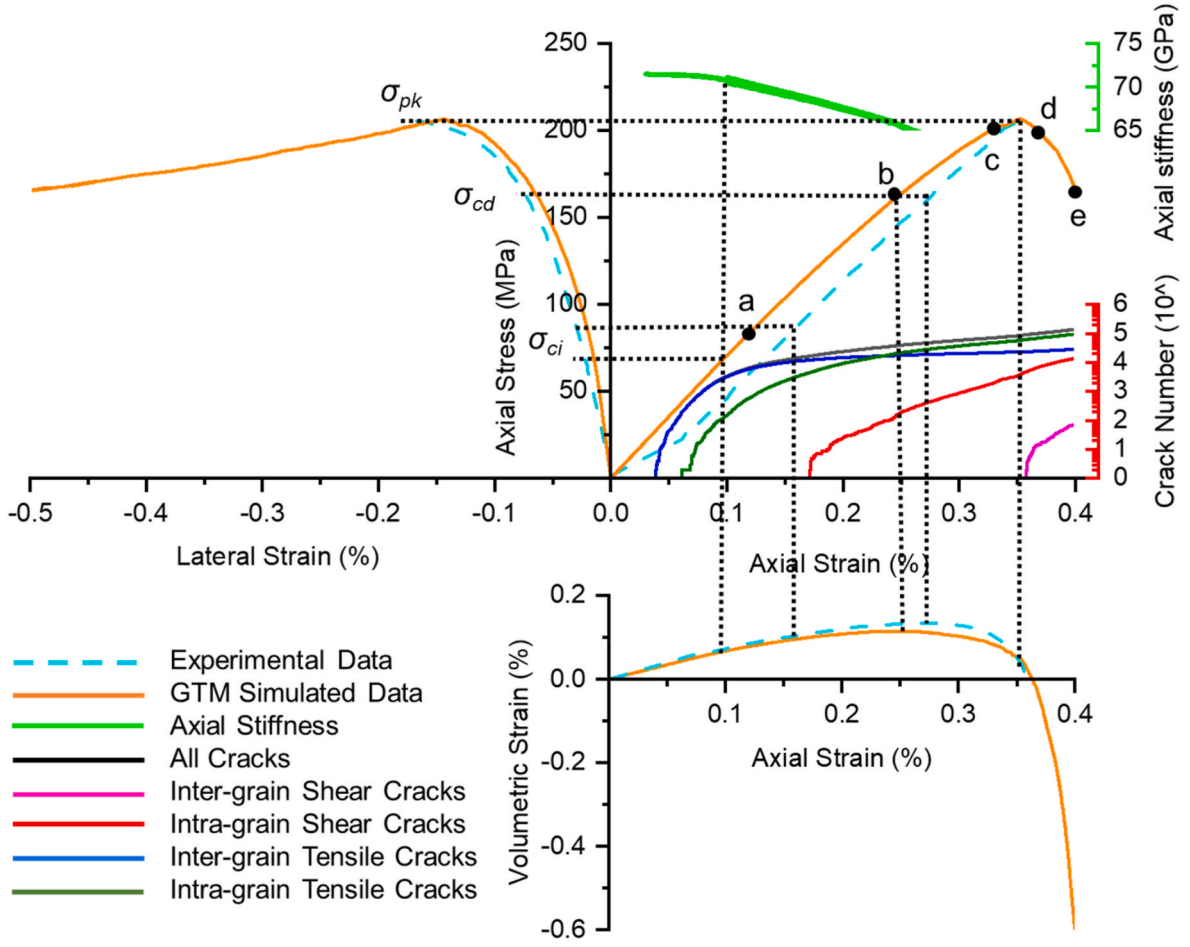

Fig. 8. Variation of axial stress, axial stiffness, the cumulative number of various crack types (log axis) and volumetric strain vs. axial strain or lateral strain of the grain texture model tested under uniaxial compression. These data are compared with the experimental data reported by Martin and Chandler.[32] Crack-initiation stress (σ_{ci}) and crack-damage stress (σ_{cd}) occur at 34% and 80% of peak strength (σ_{pk}).

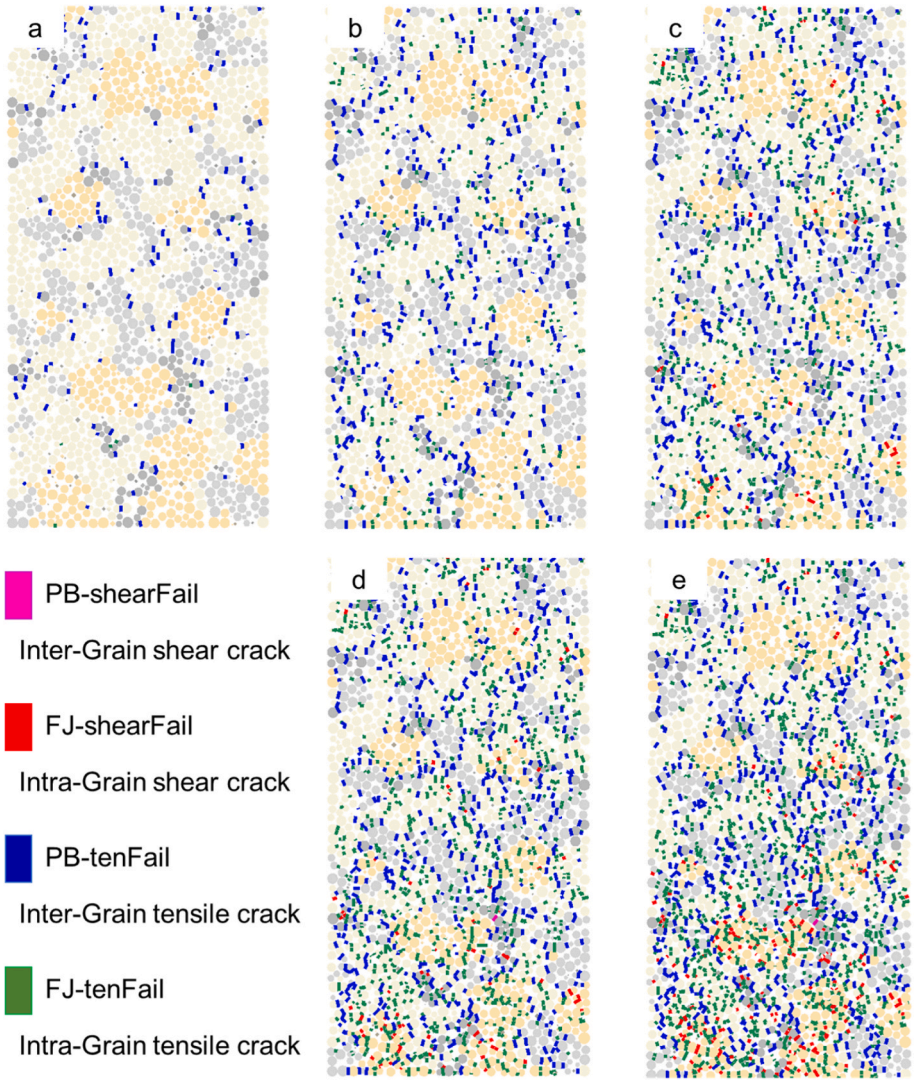

Fig. 9. Crack distributions at various stages during a uniaxial compressive test as documented in the stress-strain curve of Fig. 8: (a) Stable crack growth stage; (b) Crack-damage stress; (c) Unstable crack growth stage; (d) Post peak; (e) End of loading.

related to closure of the initial cracks and gaps, which are present in the experiment but not represented in the numerical model. Crack-initiation stress (σ_{ci}), crack-damage stress (σ_{cd}), and peak strength (σ_{pk}) are however three characteristic stress levels observed in the stress-strain curve.

The crack-initiation stress is the demarcation point between the elastic region and stable crack growth stage, where the lateral strain curve becomes nonlinear[48] and the axial stiffness curve begins to fluctuate.[15] Axial stiffness is defined as:

$$\Delta E = \frac{\sigma_a - \sigma_0}{\varepsilon_a - \varepsilon_0} \tag{9}$$

where, ΔE is axial stiffness; σ_a and ε_a are respectively the instantaneous axial stress and strain; and σ_0 and ε_0 are respectively the initial axial stress and strain. From Fig. 8, we observe that the initial point of the axial stiffness curve fluctuates at ~0.1% of axial strain, and the corresponding axial stress (71.1 MPa) in the stress-strain curve is the crack-initiation stress. The axial stiffness is of the order of 70 GPa and is equivalent to the macroscopic Young's modulus.

The crack-damage stress represents the onset of unstable crack growth, as noted by Bieniawski.[49] As shown in Fig. 8, the crack-damage stress is identified at the peak in the volumetric strain,[50] indicating the initiation of dilation.[15] The magnitude of the crack-damage stress is 164 MPa and the corresponding axial strain is 0.25%.

Peak strength at uniaxial compression (UCS) is represented by the apex of the stress-strain curve at 206.8 MPa. Thus, the numerical crack-initiation stress and crack-damage stress are respectively 34% and 80% of the UCS and compare to ~40% and ~80% in the laboratory experiments.[32] From Fig. 8, the three characteristic stress levels in the simulated results are similar to those in the experimental data, although the magnitudes of axial strain differ. This may result from ignoring the presence of initial cracks and gaps in the numerical results.

Fig. 9 shows the crack distributions at stages of crack-initiation, crack-damage and at post peak strength in the numerical uniaxial compression test. For crack-initiation results from stable tensile

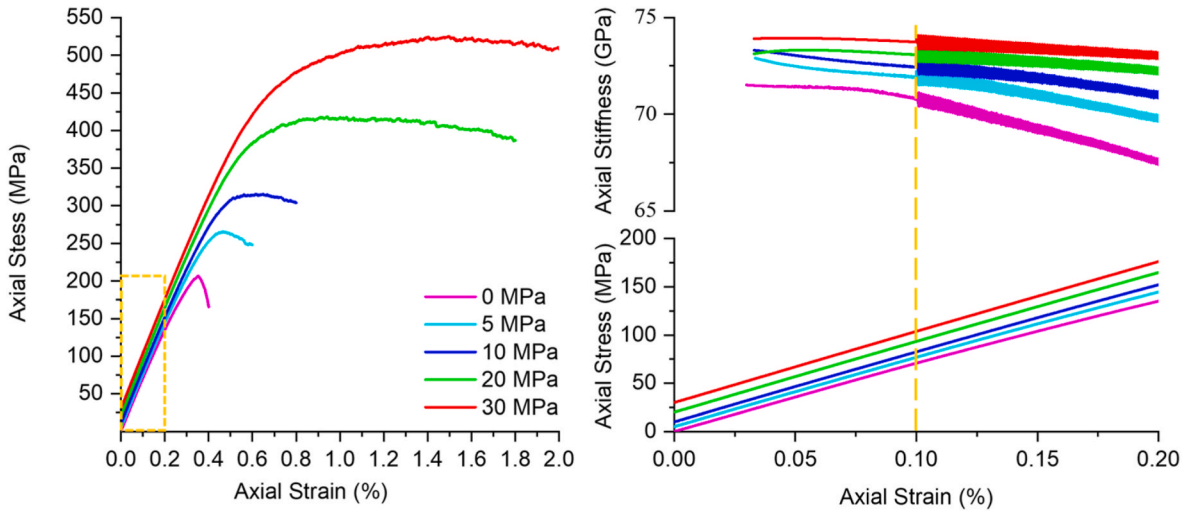

Fig. 10. Variation of axial stress vs. axial strain curves for compessive testing under various confining pressures in the left-hand-figure. Behavior at small strains noted for the dashed box of the left-hand-figure recorded at the bottom of the right-hand-figure, with axial stiffness vs. axial strain noted at the top of the right-hand-figure.

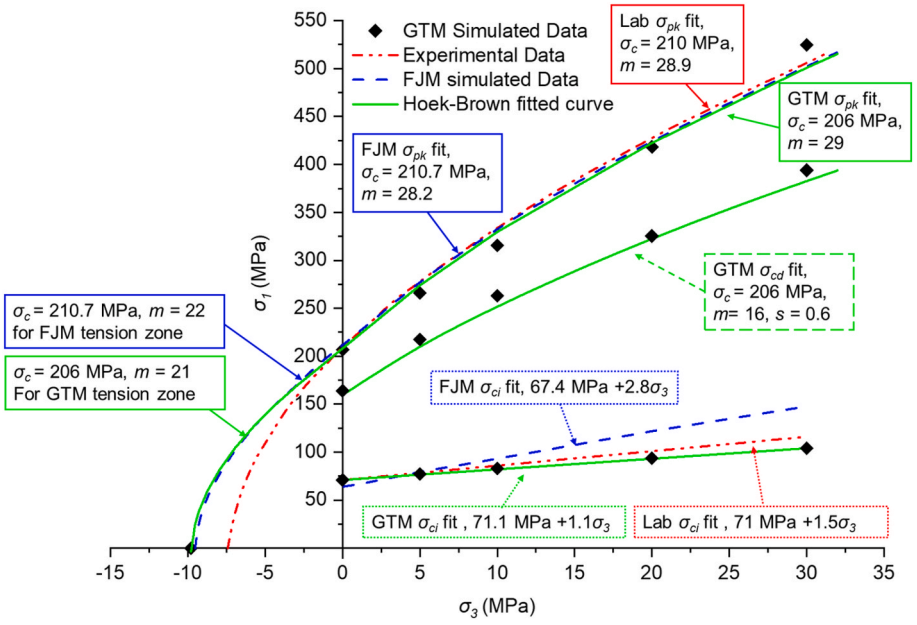

Fig. 11. Comparisons among unconfined, confined peak and crack-initiation strengths together with direct tensile strengths obtained from grain texture (GTM) and flat joint models (FJM)[27] and representing both numerical simulations and laboratory tests.[31] Fitted Hoek-Brown failure envelopes of peak strength (σ_{pk}), crack-damage stress (σ_{cd}), and crack-initiation stresses (σ_{ci}) are shown. (For interpretation of the references to color in this figure legend, the reader is referred to the Web version of this article.)

cracking,[32] numerical results show that tensile cracks mainly occur at the grain boundaries between alkali feldspar (light yellow grains) and other minerals and are distributed randomly throughout the numerical specimen (see Fig. 9 (a)). In the stable crack growth stage, tensile cracks grow rapidly both inside grains and at grain boundaries until the crack-damage stress is reached (see Fig. 9 (b)). In particular, tensile cracks at the grain boundaries between alkali feldspar (light yellow grains) and quartz (light grey grains) develop rapidly with intra-grain tensile cracks occurring mainly inside the alkali feldspars (light yellow grains). Since sliding cracks are related to the crack-damage stress,[32] shear cracks within grains increase during unstable crack growth and ultimately traverse the full grain (see Fig. 9 (c)) - mainly occurring inside the alkali feldspars (light yellow grains) and plagioclase (dark yellow grains) with relatively fewer inside the quartz (light grey grains). Shear cracks at grain boundaries begin to propagate post-peak (see Fig. 9 (d)), mainly occurring at the boundaries between quartz/biotite (light/dark grey grains) and other minerals. At the end of loading (80% of UCS), more intragrain traversing cracks propagate due to the rapid increase in length of shear cracks (see Fig. 9 (e)).

Peak strength is enhanced with an increase in confining pressure (see Fig. 10). Crack-initiation stresses under various confining pressures are represented by fluctuations in the axial stiffness vs. axial strain curves in the partially augmented figure (see the right part of Fig. 10). The crack-initiation stresses under various confining pressures are limited to

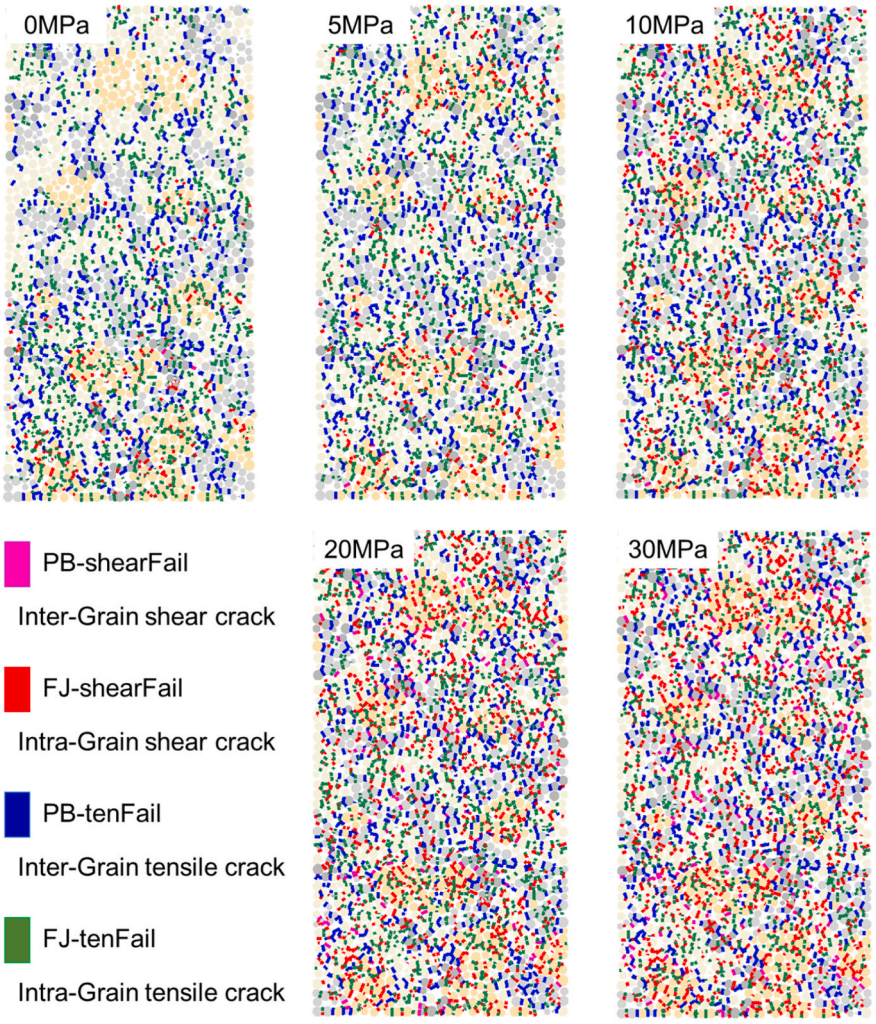

(a)

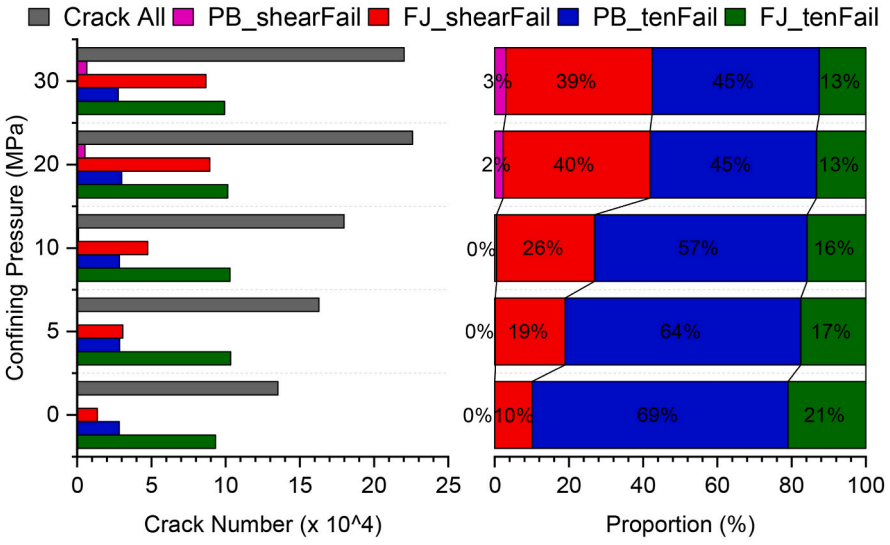

(b)

Fig. 12. Crack distributions and statistics in the post peak strength stage under various confining pressures: (a) Distribution of cracks; (b) Comparison of number and proportion of cracks over five categories.

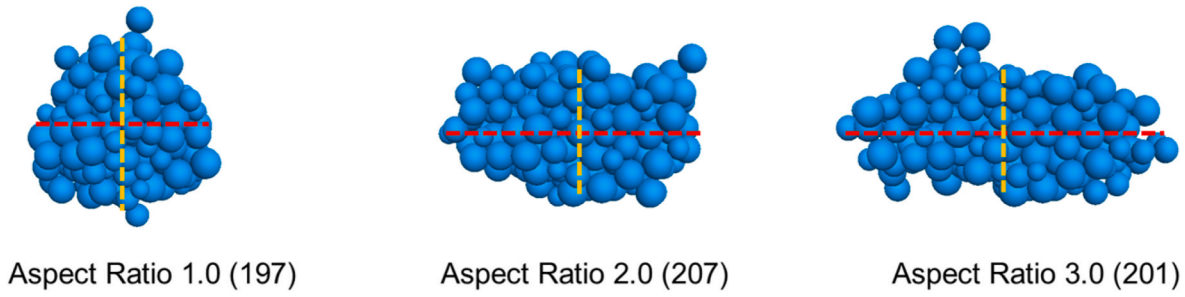

Fig. 13. Grain clusters (ID 3770) for various grain aspect ratios (number of particles shown in brackets with red dashed lines representing the long axis of the clusters, and gold dashed lines representing the short axis). (For interpretation of the references to color in this figure legend, the reader is referred to the Web version of this article.)

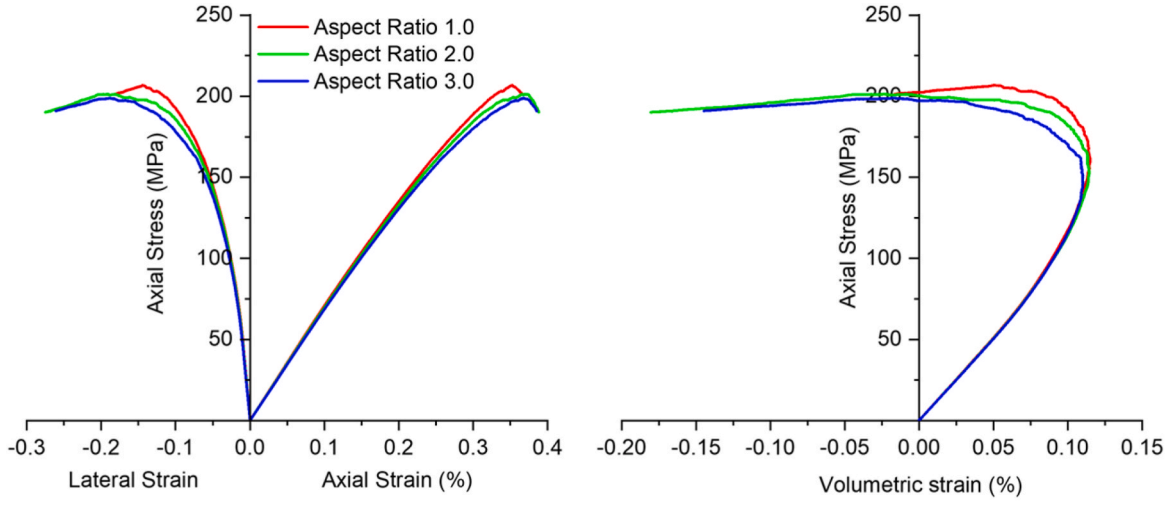

(a)

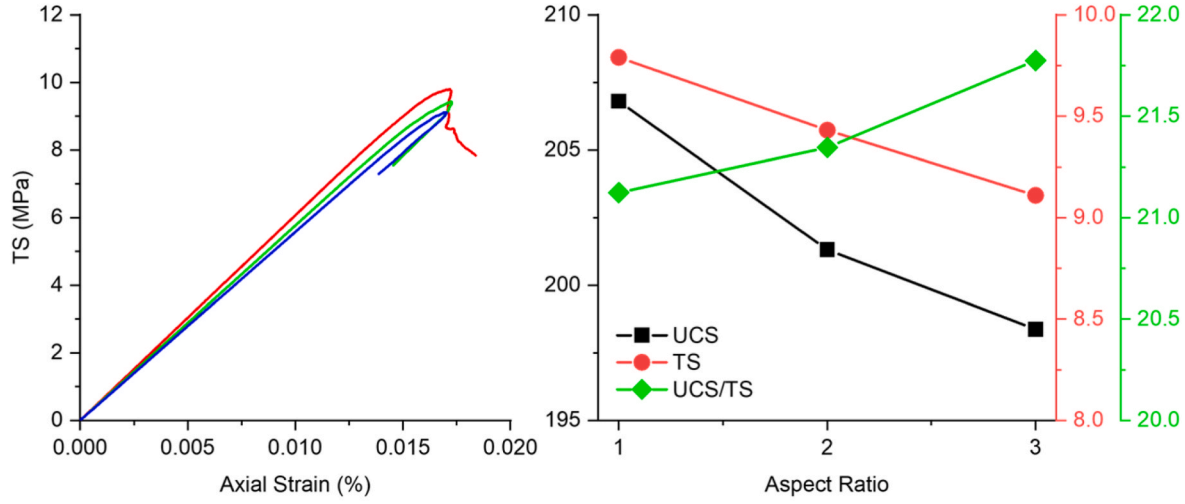

(b) (c)

Fig. 14. Simulated results with various grain aspect ratios: (a) Variation of axial stress vs. axial strain, lateral strain or volumetric strain curves for the unaxial compression tests; (b) Variation of axial stress vs. axial strain under direct tension tests; (c) Comparison of UCS, TS and the UCS/TS ratio.

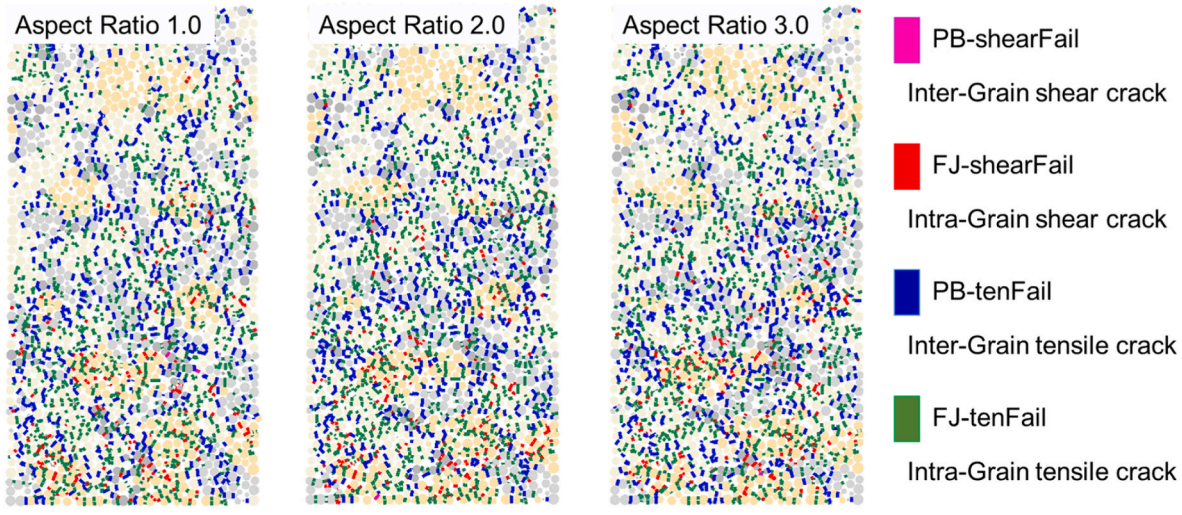

(a)

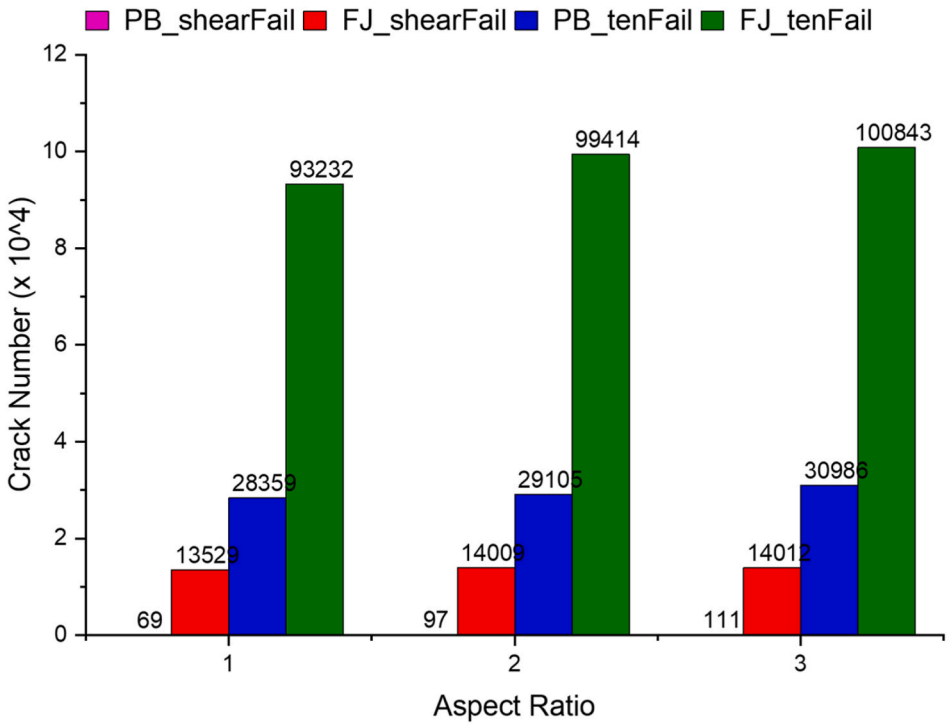

(b)

Fig. 15. Crack distributions and statistics after uniaxial compressive tests for cases with various grain aspect ratios: (a) Distribution of cracks; (b) Comparison of number of cracks.

<0.1% axial strain, and their fitted curve is linear.

The Hoek-Brown strength criterion has been widely used to describe peak strengths under various confining stresses. Martin[31] investigated the peak strengths of LdB granite and fitted Hoek-Brown failure envelopes using the parameters: $\sigma_c = 210$ MPa, $m = 28.9$ and $s = 1$. The Hoek-Brown (HB) strength criterion is defined as follows[25]

$$\sigma_1 = \sigma_3 + \sigma_c \left(m\frac{\sigma_3}{\sigma_c} + s \right)^{0.5} \tag{10}$$

where, σ_c is UCS and m and s are intrinsic material parameters representing the structure of the rock mass.

The fitted HB failure envelopes for peak strength (σ_{pk}), crack-damage stress (σ_{cd}), and crack-initiation stress (σ_{ci}) from the simulation are shown in Fig. 11, and compared with both laboratory[31] and FJM simulation results.[27] The Hoek-Brown strength criterion fitted by the GTM results are

$$\begin{array}{l} \sigma_c = 206 \text{ MPa}, \quad m = 29, \quad s = 1.0, \quad \text{for } \sigma_{pk} \\ \sigma_c = 206 \text{ MPa}, \quad m = 16, \quad s = 0.6, \quad \text{for } \sigma_{cd} \\ 71.1 \text{ MPa} + 1.1\sigma_3, \quad \text{for } \sigma_{ci} \end{array} \tag{11}$$

A crack initiation relation relevant for brittle rock has been defined by Diederichs, et al.,[50,51] as

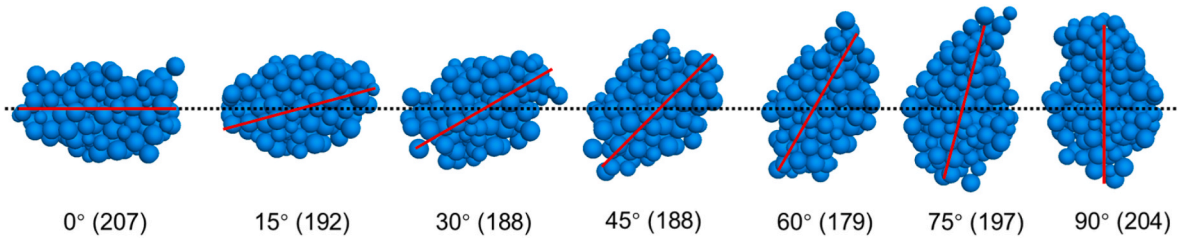

Fig. 16. Grain clusters (ID 3770) with various dip angles (number of particles in brackets, long axis as red line and dashed line representing the horizontal). (For interpretation of the references to color in this figure legend, the reader is referred to the Web version of this article.)

$$\sigma_{ci} = (0.3 \sim 0.5)\sigma_c + (1 \sim 1.5)\sigma_3 \quad (12)$$

In this work, the GTM simulated results for crack-initiation stresses can be expressed as

$$\sigma_{ci} = 0.34\sigma_c + 1.1\sigma_3 \quad (13)$$

Hence, the crack initiation law simulated by the GTM results is within the range observed by Diederichs, et al.[50,51]

For σ_{pk}, the GTM results are similar to the FJM results and both are close to the laboratory measurements. However, the crack-initiation stresses from the GTM results better approximate the laboratory data compared to the FJM results. Thus, the GTM results have successfully captured the characteristics of both crack-initiation and the peak strength failure curves.

With an increase in confining stress, the total number of cracks increases, especially for the intra-grain shear cracks (see Fig. 12(a)). Zhou, et al.[12] argued that confining pressure modulates the timing of initiation of the various crack types together with their proportion. From the number statistics of the various types of cracks shown in Fig. 12(b), it is apparent that the number of tensile cracks remains approximately constant over the range of confining stresses, but the number and proportion of shear cracks increase. The distribution of cracks (Fig. 12) indicate the enhancement in the shearing effect under increasing confining stress.

In summary, the Young's modulus, Poisson's ratio, Hoek-Brown parameter m, UCS and TS of the LdB granite calibrated for the second stage are 69.8 GPa, 0.18, 29, 206.8 MPa and 9.8 MPa, respectively. These compare favorably with the results of physical experiments listed in Table 2 - effectively replicating the observed macroscale mechanical behavior of the LdB granite.

4. Influence of grain shape and orientation

Grain shape and orientation are defined in this study by controlling the aspect ratio, dip orientation (azimuth) and dip angle of the particles. When the aspect ratio is greater than 1.0 the grain clusters become non-spherical and produce geometric anisotropy. The dip direction and dip angle of the long axis of the grain clusters define the orientation of this induced anisotropy. In this study both dip direction and dip angle of all grain clusters are assumed uniform. Uniaxial compression tests and direct tension tests are designed to study the change in the ratio of UCS to TS for these different cases.

4.1. Aspect ratio

An aspect ratio of 1 is the default for the GTM with magnitudes of 2 and 3 chosen for comparison since the average aspect ratio is 1–2.5 for granite.[40] As the aspect ratio increases from 1 to 3, representative grain clusters (group ID 3770) are shown in Fig. 13 with dip direction and dip angle of the long axis identically set to 0°.

The stress-strain response under uniaxial compression for the three GTMs with various aspect ratios are presented in Fig. 14(a). The respective UCS magnitudes for the various aspect ratios (1, 2 and 3) are 206.8 MPa, 201.3 MPa and 198.4 MPa and the respective values for corresponding crack-initiation stresses, defined for an axial strain of 0.1%, are 71.1 MPa, 69.9 MPa and 68.9 MPa. All the GTMs exhibit similar elastic deformation before reaching the crack-initiation stress. From the crack-initiation stress to peak strength, the lateral strain curves diverge among specimens which are ultimately associated with a spectrum of peak strengths. The results of the direct tension tests are presented in Fig. 14(b), and the respective tensile strength (TS) magnitudes are 9.8 MPa, 9.4 MPa and 9.1 MPa for aspect ratios of 1–3. Fig. 14(c) shows that when aspect ratio increases from 1 to 3 the UCS and TS are both reduced, but the ratio of UCS to TS increases slightly. The increasing UCS/TS ratio indicates that the aspect ratio has a greater effect on tensile strength than shear strength in GTMs.

Regardless of the distribution of grain clusters, the failure modes of the three groups for different aspect ratios are similar (see Fig. 15 (a)). Comparing the number of various crack types (Fig. 15(b)) shows that the number increases with an increase in aspect ratio, for all crack types, but especially for tensile cracks both inside the grain and at the grain boundary. For shear cracks, the number of intra-grain cracks changes only slightly with aspect ratio whereas the number of inter-grain cracks is sensitive to this.

4.2. Dip angle

We examine the sensitivity to orientation of the minerals by retaining the dip direction at 0° but increasing the dip angle from 0° to 90° in intervals of 15°. Representative grain clusters with various dip angles are shown in Fig. 16 for an aspect ratio of 2.

The change in dip angle exerts little influence on failure mode (see Fig. 17(a)) but changes the number of various crack types (see Fig. 17 (b)) and the strengths for both UCS and TS loading experiments (see Fig. 17(c)) with the GTMs. With an increase in dip angle from 0° to 90°, the number of intra-grain cracks trends to reduce while the number of inter-grain tensile cracks continues to increase. UCS increases with an increase in dip angle with a dip of 0° being weaker than the other cases. TS increases dramatically with an increase in dip angle, resulting in a reduction in the UCS/TS ratio from 21 to 17. This indicates that grain orientation has a significant influence on the micromechanical behavior.

5. Discussion

The change in grain shape from spherical to ellipsoidal exerts a

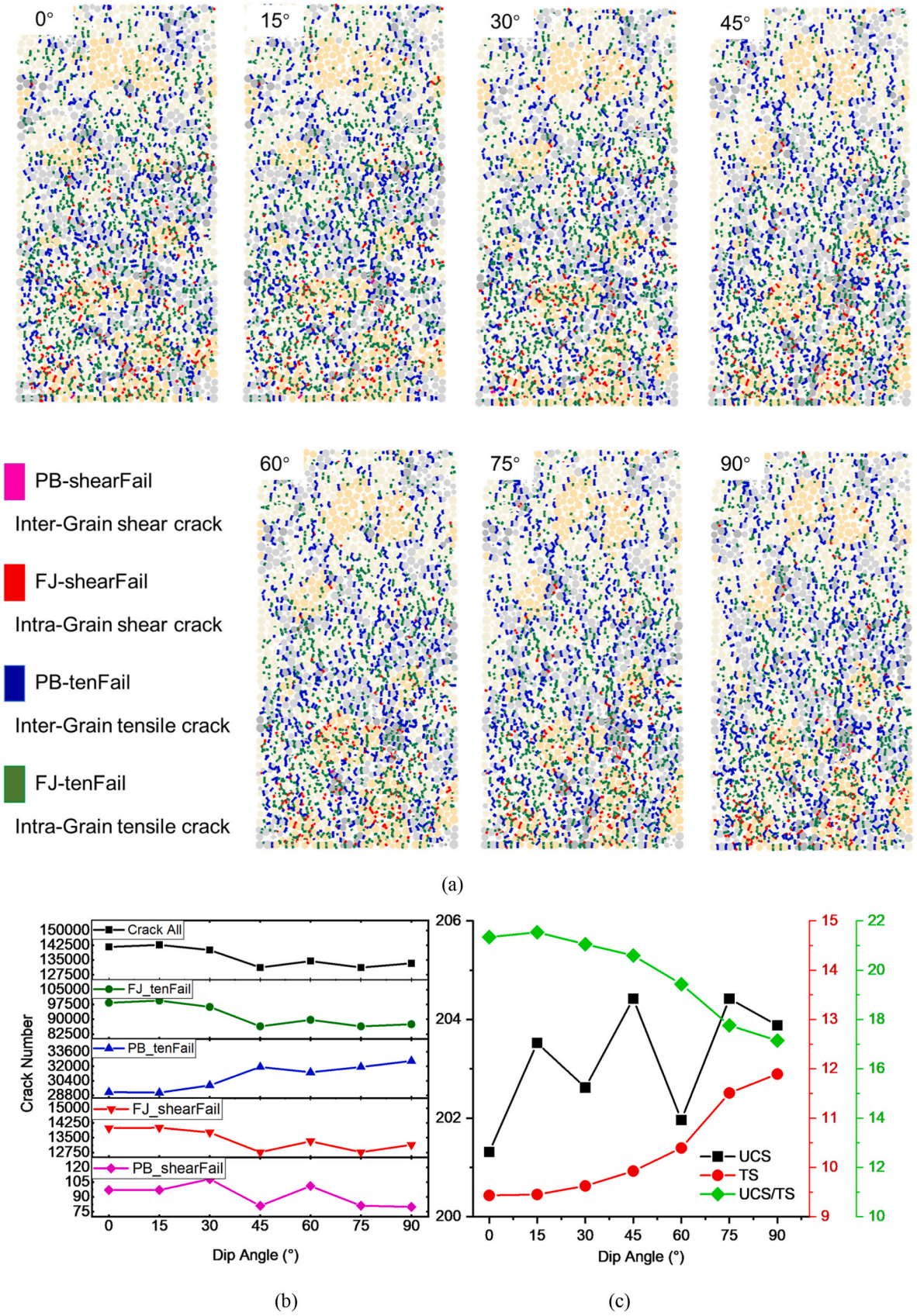

Fig. 17. Simulated results for various dip angles of the grain clusters: (a) Distribution of cracks; (b) Comparison of number of cracks; (c) Comparison of UCS, TS and the UCS/TS ratio.

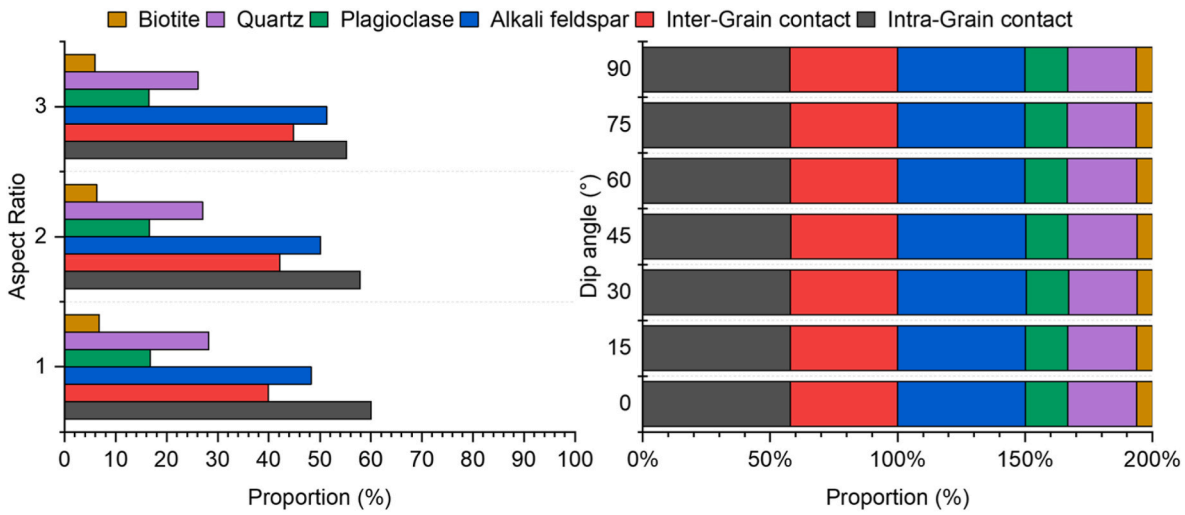

Fig. 18. Proportion of various minerals and contact types for grain texture models (GTMs) in the cases of various aspect ratios and dip angles.

significant influence on the macro-mechanical properties of the GTM. Previous studies[9,12,13] considered only a change in the proportion of mineral groups but the proportion of contact groups is not discussed. We define the statistics of the change in the proportion of mineral groups and contact groups used in Section 4 as shown in Fig. 18.

Fig. 18 shows that a change in aspect ratio exerts only a small influence on the proportion of mineral groups during the discretization process, but the proportion of inter-grain contacts increases from 55% to 60% as the aspect ratio transits from 1 to 3. The reason for this is apparent from Eq. (5) (see Section 2.3). The volume of the substituted ellipsoid (V_{ed}) is equal to the volume of the original sphere (V_{sp}), although the surface area of the ellipsoid (A_{ed}) is not equal to the surface area of the sphere (A_{sp}), as follows

$$\begin{aligned} &\text{For } a = \lambda^2 R,\ \ b = c = \lambda^{-1} R, \\ &V_{sp} = \frac{4}{3}\pi R^3,\ \ V_{ed} = \frac{4}{3}\pi abc,\ \ V_{sp} = V_{ed} \\ &A_{sp} = 4\pi R^2,\ \ A_{ed} = \frac{4}{3}\pi(ab + bc + ac),\ \ A_{ed} = \left(\frac{2}{3}\lambda + \frac{1}{3}\lambda^{-2}\right)A_{sp} \end{aligned} \tag{14}$$

Thus, when $\lambda > 1$, $A_{sp} < A_{ed}$ and A_{ed} increases with an increase in λ, which in-turn leads to an increase in inter-grain contacts. Since the inter-grain contacts are weaker than the intra-grain contacts, the UCS and TS (Section 4.1) reduce with an increase in the aspect ratio. In contrast, a change in dip angle does not change the proportion of either the mineral groups or the contact groups (the right part in Fig. 18). However, dip angle does have a significant influence on the number of inter-grain tensile cracks and the resulting UCS/TS ratio, indicating the significant control of the grain texture.

6. Conclusions

For textured crystalline rocks, grain size, shape, and orientation exert an important influence on micro-mechanical response. Conventional grain-based models (GBMs) typically only account for grain size and dismiss the role of grain aspect ratio and orientation that contribute to overall anisotropy of the rock as unimportant. Conversely, we employ clumped grain models to study the effect of grain shape and orientation and distinguish between inter-grain and intra-grain failure modes in crystalline rock. Such grain texture models (GTMs) provide insight into the evolution of damage in and around real mineral grains by producing random-irregular forms representative of real mineral grains. Hence, the presented GTMs combine the advantages of GBMs and clumped particle methods and overcome their principal limitations.

A detailed calibration procedure of the GTM is completed and direct tension, uniaxial, and triaxial compression tests are completed on the numerical specimens. The evolution of crack damage formation and propagation observed within the numerical specimen during loading is similar to observations in real samples.[31] With an increase in confining stress, the failure mode transitions from axial splitting to predominantly shear failure. The fitted Hoek-Brown strength envelopes for peak strength and crack-initiation stresses are also consistent with the physical experiments. The fitted crack-initiation stresses are more closely matched than those simulated using flat joint models (FJMs), alone. This is the first time that a 3D DEM model based on grain texture has been shown to capture the major macro-mechanical characteristics of textured rock inclusive of matching the UCS/TS ratio, failure process, nonlinear strength envelope and failure mode.

The influence of grain shape and orientation on strength and deformability is evaluated for grains of various aspect ratios and for different dip angles of these grains. An increase in aspect ratio both decreases UCS and TS but slightly increase the UCS/TS ratio. An increase in dip angle from 0° to 90° increases TS dramatically and decreases the UCS/TS ratio from 21 to 17. By analyzing the proportion of mineral groups and contact groups, we find that an increase in grain aspect ratio increases the proportion of inter-grain contacts. In contrast, the change in dip angle has little influence on the proportion of either the mineral groups or the contact groups, but exerts a significant influence on the number of inter-grain tensile cracks and the resulting UCS/TS ratio. Thus, we conclude that grain anisotropy texture exerts a significant control on the macro-mechanical behavior of rock.

Declaration of competing interest

The authors declare that they have no known competing financial interests or personal relationships that could have appeared to influence the work reported in this paper.

Acknowledgments

The work reported in this paper was financially supported by the National Natural Science Foundation of China (NSFC) under Contract no. 51428902.

Appendix A

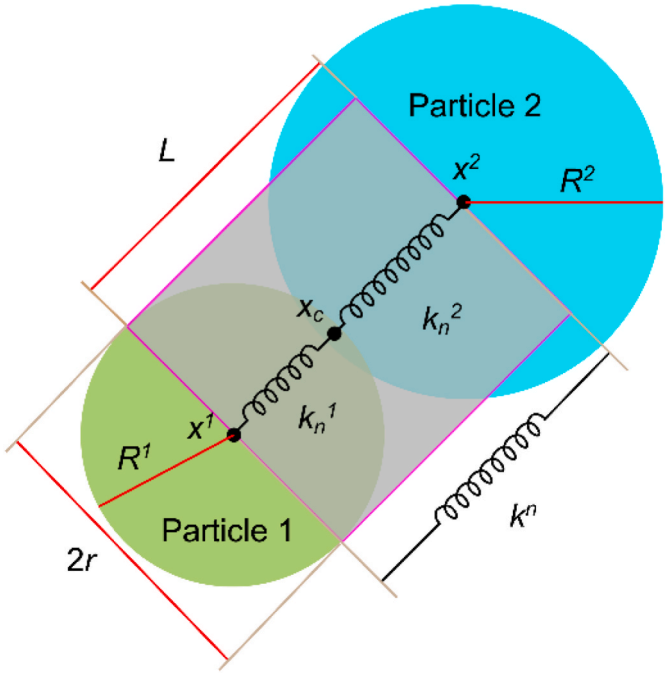

Fig. A1. Relation between normal stiffness and normal particle stiffnesses for the linear model (x^1, x^2 and x_c are the locations of the center points of particles *1*, *2* and the particle-particle contact, respectively).

In previous studies, the elastic parameters of the contact are calculated by the normal and shear stiffnesses of the connected particles. However, the contact stiffness is not truly independent of particle size. We define new formulae to evaluate the elastic parameters from the elastic modulus of the aggregate materials and present the derivation in Eq. (7).

In granular mechanics codes, for particle-particle contacts, the elastic modulus, normal and shear stiffnesses, and normal to shear stiffness ratio are E_c, k^n, k^s, k_c, respectively. The radius, normal and shear particle stiffnesses of the contacting particle are R^i, $k_n{}^i$, $k_s{}^i$, where i is the particle index with values of *1* or *2*.

The relationship between normal stiffness and elastic modulus is as shown in Fig. A1 and Eq. (A1) [52]:

$$k^n = \frac{AE_c}{L},\quad k^s = \frac{k^n}{k_c}$$
$$\text{with}\quad A = \pi r^2\quad (3D),$$
$$r = \begin{cases} \min\left(R^1,\ R^2\right), & \text{for contact} \\ R^i, & \text{for particle} \end{cases}, \tag{A1}$$
$$L = \begin{cases} R^1 + R^2, & \text{for contact} \\ R^i, & \text{for particle} \end{cases}.$$

where, A, r and L are area, average radius and length of the contact or particle, respectively. The contact stiffness is inherited from the particle stiffnesses as[52]

$$\frac{1}{k^n} = \frac{1}{k_n^1} + \frac{1}{k_n^2}$$
$$\frac{1}{k^s} = \frac{1}{k_s^1} + \frac{1}{k_s^2} \tag{A2}$$

Next, we substitute Eq. (A1) into Eq. (A2):

$$\frac{R^1 + R^2}{\pi r^2 E_c} = \frac{R^1}{\pi\left(R^1\right)^2 E_1} + \frac{R^2}{\pi\left(R^2\right)^2 E_2}$$
$$\frac{R^1 + R^2}{\pi r^2 E_c} k_c = \frac{R^1}{\pi\left(R^1\right)^2 E_1} k_1 + \frac{R^2}{\pi\left(R^2\right)^2 E_2} k_2 \tag{A3}$$

Thus, we obtain from Eq. (A3):

$$E_c = \frac{R^1 + R^2}{r^2}\frac{R^1 R^2 E_1 E_2}{R^2 E_1 + R^1 E_2}$$
$$k_c = \frac{r^2 E_c}{\left(R^1 + R^2\right)}\left(\frac{1}{R^1 E_1}k_1 + \frac{1}{R^2 E_2}k_2\right) \quad \text{(A4)}$$

Since the elastic modulus is independent of particle size then Eq. (A2) should be exact in the case that $R^1 = R^2$. Thus, we obtain a general solution from Eq. (A4) as:

$$E_c = \frac{2E_1 E_2}{E_1 + E_2}$$
$$k_c = \frac{k_1 E_2 + k_2 E_1}{E_1 + E_2} \quad \text{(A5)}$$

Finally, we can verify that Eq. (A5) is correct by assuming contacting particles to belong to the same material, such that $E_1 = E_2$, $k_1 = k_2$. Then, $E_c = E_1 = E_2$, $k_c = k_1 = k_2$.

References

1 Potyondy DO. Simulating stress corrosion with a bonded-particle model for rock. *Int J Rock Mech Min.* 2007;44(5):677–691.
2 Pyle DM, Lu J, Littlewood DJ, Maniatty AM. Effect of 3D grain structure representation in polycrystal simulations. *Comput Mech.* 2013;52(1):135–150.
3 Potyondy DO. A grain-based model for rock: approaching the true microstructure. In: *Paper Presented at: In Proceedings of Bergmekanikk I Norden 2010 — Rock Mechanics in the Nordic Countries*. 2010. June 9–12, 2010, 2010; Kongsberg, Norway.
4 Ghazvinian E, Diederichs MS, Quey R. 3D random Voronoi grain-based models for simulation of brittle rock damage and fabric-guided micro-fracturing. *J Rock Mech Geotech.* 2014;6(6):506–521.
5 Hofmann H, Babadagli T, Zimmermann G. A grain based modeling study of fracture branching during compression tests in granites. *Int J Rock Mech Min.* 2015;77:152–162.
6 Gao F, Stead D, Elmo D. Numerical simulation of microstructure of brittle rock using a grain-breakable distinct element grain-based model. *Comput Geotech.* 2016;78:203–217.
7 Li XF, Li HB, Zhao Y. 3D polycrystalline discrete element method (3PDEM) for simulation of crack initiation and propagation in granular rock. *Comput Geotech.* 2017;90:96–112.
8 Peng J, Wong LNY, Teh CI. Effects of grain size-to-particle size ratio on micro-cracking behavior using a bonded-particle grain-based model. *Int J Rock Mech Min.* 2017;100:207–217.
9 Wong LNY, Peng J, Teh CI. Numerical investigation of mineralogical composition effect on strength and micro-cracking behavior of crystalline rocks. *J Nat Gas Sci Eng.* 2018;53:191–203.
10 Li XF, Zhang QB, Li HB, Zhao J. Grain-based discrete element method (GB-DEM) modelling of multi-scale fracturing in rocks under dynamic loading. *Rock Mech Rock Eng.* 2018;51(12):3785–3817.
11 Li H, Yang C, Ma H, Shi X, Zhang H, Dong Z. A 3D grain-based creep model (3D-GBCM) for simulating long-term mechanical characteristic of rock salt. *J Petrol Sci Eng.* 2020:185.
12 Zhou J, Lan HX, Zhang LQ, Yang DX, Song J, Wang S. Novel grain-based model for simulation of brittle failure of Alxa porphyritic granite. *Eng Geol.* 2019;251:100–114.
13 Hofmann H, Babadagli T, Yoon JS, Zang A, Zimmermann G. A grain based modeling study of mineralogical factors affecting strength, elastic behavior and micro fracture development during compression tests in granites. *Eng Fract Mech.* 2015;147:261–275.
14 Cho N, Martin CD, Sego DC. A clumped particle model for rock. *Int J Rock Mech Min.* 2007;44(7):997–1010.
15 Yoon JS, Zang A, Stephansson O. Simulating fracture and friction of Aue granite under confined asymmetric compressive test using clumped particle model. *Int J Rock Mech Min.* 2012;49:68–83.
16 Zhang Q, Zhu H-H, Zhang L. Studying the effect of non-spherical micro-particles on Hoek-Brown strength parametermiusing numerical true triaxial compressive tests. *Int J Numer Anal Met.* 2015;39(1):96–114.
17 Ye Y, Thoeni K, Zeng Y, Buzzi O, Giacomini A. A novel 3D clumped particle method to simulate the complex mechanical behavior of rock. *Int J Rock Mech Min.* 2019;120:1–16.
18 Åkesson U. *Characterisation of Micro Cracks Caused by Coredisking*. Swed: SKB; 2008:8–103.
19 Potyondy DO. The bonded-particle model as a tool for rock mechanics research and application: current trends and future directions. *Geosystem Eng.* 2015;18(1):1–28.
20 Wang T, Zhou W, Chen J, Xiao X, Li Y, Zhao X. Simulation of hydraulic fracturing using particle flow method and application in a coal mine. *Int J Coal Geol.* 2014;121:1–13.
21 Potyondy DO. Flat-joint contact model [version 1]. In: *Technical Memorandum 5-8106*. Minneapolis, MN: Itasca Consulting Group, Inc.; 2016:16TM47.
22 Wang T, Hu WR, Elsworth D, et al. The effect of natural fractures on hydraulic fracturing propagation in coal seams. *J Petrol Sci Eng.* 2017;150:180–190.
23 Mehranpour MH, Kulatilake PHSW. Improvements for the smooth joint contact model of the particle flow code and its applications. *Comput Geotech.* 2017;87:163–177.
24 Potyondy DO, Cundall PA. A bonded-particle model for rock. *Int J Rock Mech Min.* 2004;41(8):1329–1364.
25 Scholtès L, Donzé F-V. A DEM model for soft and hard rocks: role of grain interlocking on strength. *J Mech Phys Solid.* 2013;61(2):352–369.
26 Potyondy DO. A flat-jointed bonded-particle material for hard rock. In: *Paper Presented at: Proceedings of 46th U.S. Rock Mechanics/Geomechanics Symposium*. 2012. June, (Chicago, USA).
27 Li K, Cheng Y, Fan X. Roles of model size and particle size distribution on macro-mechanical properties of Lac du Bonnet granite using flat-joint model. *Comput Geotech.* 2018;103:43–60.
28 Potyondy DO. *Material-Modeling Support for PFC [fistPkg26]*. Minneapolis, MN: Itasca Consulting Group, Inc.; 2018. August 24.
29 Itasca Consulting Group, Inc.. *FISH IN PFC3D. PFC3D—Particle Flow Code in 3 Dimensions, Version 4*. Itasca Consulting Group, Inc.; 2008. Minneapolis, MN, USA.
30 Cox MR, Budhu M. A practical approach to grain shape quantification. *Eng Geol.* 2008;96(1-2):1–16.
31 Martin CD. *The Strength of Massive Lac du Bonnet Granite Around Underground Openings* [Ph.D. thesis]. University of Manitoba; 1993.
32 Martin CD, Chandler NA. The progressive fracture of lac du Bonnet granite. *Int J Rock Mech Min Sci.* 1994;31(6):643–659.
33 Martin CD. Seventeenth Canadian geotechnical colloquium: the effect of cohesion loss and stress path on brittle rock strength. *Can Geotech J.* 1997;34(5):698–725.
34 Wang Y, Tonon F. Modeling Lac du Bonnet granite using a discrete element model. *Int J Rock Mech Min.* 2009;46(7):1124–1135.
35 Howarth DF, Rowlands JC. Quantitative assessment of rock texture and correlation with drillability and strength properties. *Rock Mech Rock Eng.* 1987;20(1):57–85.
36 He W, Hayatdavoudi A, Shi H, Sawant K, Huang P. A preliminary fractal interpretation of effects of grain size and grain shape on rock strength. *Rock Mech Rock Eng.* 2018;52(6):1745–1765.
37 Mock A, Jerram DA. Crystal size distributions (CSD) in three dimensions: insights from the 3D reconstruction of a highly porphyritic rhyolite. *J Petrol.* 2005;46(8):1525–1541.
38 Sen K, Mamtani MA. Magnetic fabric, shape preferred orientation and regional strain in granitic rocks. *J Struct Geol.* 2006;28(10):1870–1882.
39 Okamoto A, Sekine K. Textures of syntaxial quartz veins synthesized by hydrothermal experiments. *J Struct Geol.* 2011;33(12):1764–1775.
40 Karsli F, Dihkan M. An image analysis method to detect CSD on rocks with adjusted color images. *Sens Rev.* 2013;33(4):323–340.
41 Nicco M, Holley EA, Hartlieb P, Pfaff K. Textural and mineralogical controls on microwave-induced cracking in granites. *Rock Mech Rock Eng.* 2020;53(10):4745–4765.
42 Bass JD. Elasticity of minerals, glasses, and melts. In: *Mineral Physics & Crystallography*. 1995:45–63.
43 Simmons G, Wang H. *Single Crystal Elastic Constants and Calculated Aggregate Properties: A Handbook*. 1971. Handbook.
44 Chen S, Yue ZQ, Tham LG. Digital image-based numerical modeling method for prediction of inhomogeneous rock failure. *Int J Rock Mech Min.* 2004;41(6):939–957.

45 Villeneuve M. *Examination Of Geological Influence On Machine Excavation Of Highly Stressed Tunnels In Massive Hard Rock* [Ph.D thesis]. Queen's University; 2008.
46 Chen W, Konietzky H. Simulation of heterogeneity, creep, damage and lifetime for loaded brittle rocks. *Tectonophysics*. 2014;633:164–175.
47 Yang C, Xiong Y, Wang J, Li Y, Jiang W. Mechanical characterization of shale matrix minerals using phase-positioned nanoindentation and nano-dynamic mechanical analysis. *Int J Coal Geol*. 2020:229.
48 Ghazvinian E, Diederichs MS, Labrie D, Martin CD. An investigation on the fabric type dependency of the crack damage thresholds in brittle rocks. *Geotech Geol Eng*. 2015;33(6):1409–1429.
49 Bieniawski ZT. Mechanism of brittle fracture of rock: Part II—experimental studies. *Int J Rock Mech Min Sci*. 1967;4(4):407–423.
50 Diederichs MS, Kaiser PK, Eberhardt E. Damage initiation and propagation in hard rock during tunnelling and the influence of near-face stress rotation. *Int J Rock Mech Min*. 2004;41(5):785–812.
51 Diederichs MS. Manuel Rocha Medal recipient - rock fracture and collapse under low confinement conditions. *Rock Mech Rock Eng*. 2003;36(5):339–381.
52 Itasca Consulting Group, Inc.. *PFC3D-Particle Flow Code in 3 Dimensions, Version 5*. Itasca Consulting Group, Inc.; 2014. Minneapolis, MN, USA.